ATP13A2 deficiency disrupts lysosomal polyamine export

Sarah van Veen[1#], Shaun Martin[1#], Chris Van den Haute[2,3], Veronick Benoy[1], Joseph Lyons[4], Roeland Vanhoutte[5], Jan Pascal Kahler[5], Jean-Paul Decuypere[1,6,7,8], Géraldine Gelders[2], Eric Lambie[9,10], Jeffrey Zielich[9], Johannes V. Swinnen[6], Wim Annaert[7], Patrizia Agostinis[8,11], Bart Ghesquière[12], Steven Verhelst[5,13], Veerle Baekelandt[2], Jan Eggermont[1], Peter Vangheluwe*[1]

[1]Laboratory of Cellular Transport Systems, [5]Laboratory of Chemical Biology, [8]Laboratory of Cell Death Research & Therapy, Department of Cellular and Molecular Medicine, KU Leuven, Leuven, Belgium

[2]Laboratory for Neurobiology and Gene Therapy, Department of Neurosciences, [3]Leuven Viral Vector Core, KU Leuven, Leuven, Belgium

[4]Department of Molecular Biology and Genetics – DANDRITE, Aarhus, Denmark

[6]Laboratory of Lipid Metabolism and Cancer, Department of Oncology, LKI – Leuven Cancer Institute, KU Leuven, Leuven, Belgium

[7]Laboratory of Membrane Trafficking (VIB-KU Leuven Center for Brain & Disease Research), Department of Neurosciences, KU Leuven, Leuven, Belgium

[9]Cell and Developmental Biology, Department Biology II, Ludwig-Maximilians-Universtät Münich, Germany

[10]Department of Cell and Developmental Biology, University College London, UK

[11]VIB-KU Leuven Center for Cancer Biology, Department of Oncology, KU Leuven, Leuven, Belgium

[12]Metabolomics Expertise Center (VIB-KU Leuven Center for Cancer Biology), Department of Oncology, KU Leuven, Leuven, Belgium

[13]Leibniz Institute for Analytical Sciences ISAS, Otto-Hahn-Str. 6b, 44227 Dortmund, Germany

 # Authors have equally contributed

Corresponding author:

Prof. Dr. Peter Vangheluwe

Department of Cellular and Molecular Medicine

KU Leuven Campus Gasthuisberg, O&N I Herestraat 49 - box 802, 3000 Leuven

Tel.: +32 16 33 07 20

E-mail: peter.vangheluwe@kuleuven.be

ATP13A2 (PARK9) is a late endo-lysosomal transporter of unknown function that is genetically implicated in a spectrum of neurodegenerative disorders, including Kufor-Rakeb syndrome, a parkinsonism with dementia[1] and early-onset Parkinson's disease (PD)[2]. ATP13A2 offers protection against genetic and environmental risk factors of PD, whereas loss of ATP13A2 compromises lysosomal function[3]. The lysosomal transport function of ATP13A2 remained unclear, but here, we establish ATP13A2 as a lysosomal polyamine exporter with highest affinity for spermine. Polyamines stimulate the activity of purified ATP13A2, while disease mutants are functionally impaired to a degree that correlates with the disease phenotype. ATP13A2 promotes cellular polyamine uptake via endocytosis and transports polyamines into the cytosol, which highlights a role for endo-lysosomes in cellular polyamine uptake. At high concentrations, polyamines induce cell toxicity, which is exacerbated by ATP13A2 loss due to lysosomal dysfunction, lysosomal rupture and cathepsin B activation. This phenotype is recapitulated in neurons and nematodes with loss of ATP13A2 or its orthologues. Thus, defective lysosomal polyamine export is a new mechanism for lysosome-dependent cell death that may be implicated in neurodegeneration. Our findings further shed light on the molecular identity of the elusive mammalian polyamine transport system.

ATP13A2 is a P5B-ATPase belonging to the family of P-type ATPases, which couple ATP hydrolysis to substrate transport while transiently forming a catalytic phospho-intermediate[4]. ATP13A2 is generally described as a heavy metal transporter[5], but Ca^{2+} [6] and the polyamine spermidine (SPD)[7,8] were also proposed. To screen for the transported substrate(s) of ATP13A2, we measured ATPase activity in the presence of various candidate substrates in solubilized microsomal membrane fractions of SH-SY5Y cells that overexpress human ATP13A2 wild type (WT) (WT-OE) or comparable levels of the catalytically dead D508N mutant (D508N-OE)[9,10].

ATPase activity of ATP13A2 WT was significantly stimulated by the polyamines SPD and spermine (SPM) (Fig. 1a), whereas SPM had no effect on the D508N mutant (Extended Data Fig. 1a). $MnCl_2$, $ZnCl_2$, $FeCl_3$, $CaCl_2$, diamines, monoamines and amino acids exerted no effect (Extended Data Fig. 1a-

d). The polyamines SPM, N^1-acetylspermine and SPD were able to stimulate ATPase activity in a concentration-dependent manner (Fig. 1b, Extended Data Fig. 1e) with the highest apparent affinity for SPM (Extended Data Table 1).

The catalytic auto-phosphorylation and/or dephosphorylation reactions of P-type ATPases occur in response to binding of the transported substrate[4]. ATP13A2 forms a phospho-intermediate on the D508 residue in the absence of SPM supplementation[9,10], whereas SPM leads to a dose-dependent reduction in ATP13A2 phospho-enzyme levels (Fig. 1c), which is not seen with ornithine (Extended Data Fig. 1f). The dephosphorylation rate following a chase with non-radioactive ATP increased in the presence of SPM (Fig. 1d), further indicating that SPM may be the transported substrate.

SPM also stimulated the ATPase activity of purified human ATP13A2 (purification: Extended Data Fig. 2a-e). However, purified ATP13A2 only presented similar properties as microsomal ATP13A2 in the presence of the regulatory lipids phosphatidylinositol(3,5)bisphosphate (PI(3,5)P2) and phosphatidic acid (PA), which bind to the N-terminus of ATP13A2[9-11] (Fig. 1e-f, Extended Data Fig. 2f, Extended Data Table 1). SPM-induced ATPase activity was blocked by orthovanadate, a general P-type ATPase inhibitor (Extended Data Fig. 1g). Finally, we also purified the ATP13A2 mutant E343A, carrying a mutation in the conserved catalytic motif for dephosphorylation (^{341}TGES) (Extended Data Fig. 2g). The E343A mutant underwent auto-phosphorylation (Fig. 1g), but displayed limited SPM-induced ATPase activity (Extended Data Fig. 2h). Importantly, when the phospho-enzyme was chased with cold ATP, SPM clearly stimulated dephosphorylation of purified WT, but not of the E343A mutant (Fig. 1g, Extended Data Fig. 1h and 6a).

ATP13A2 is a lysosomal polyamine exporter

Next, we performed transport assays with ^{3}H-labelled SPM (^{3}H-SPM) in reconstituted vesicles from solubilized yeast membranes expressing BAD-labelled ATP13A2 WT or E343A, supplemented with the activating lipid PA. This reconstitution rendered two populations of ATP13A2 proteins that were either inserted right-side-out (ATP-binding domain in the extra-luminal space) or inside-out (ATP-binding domain in the lumen) (Fig. 1h-i). Uptake of ^{3}H-SPM was only detected for ATP13A2 WT, but not the E343A mutant, when ATP was present inside the vesicles, together with an ATP-regenerating

system (Fig. 1j), *i.e.* when ATP13A2 was positioned inside-out ((2) in Fig. 1h). Extending these insights to the cellular context, where ATP13A2 is present in the late endo-lysosomal compartment[1,12], ATP13A2 most likely operates as a lysosomal SPM exporter.

Interestingly, ATP13A2 functionality impacts on the cellular polyamine content. Indeed, we generated two independent ATP13A2 knock-out SH-SY5Y cell lines by CRISPR/Cas9 genome editing (KO, Extended Data Fig. 3a) and demonstrated via mass spectrometry that the total cell content of polyamines was lower in KO than in control (CON) cells (Fig. 2a). Expression in the KO background of ATP13A2 WT (KO/WT) for rescue or the D508N mutant (KO/D508N) as negative control (Extended Data Fig. 3b) resulted in a significantly higher SPD and SPM content in KO/WT cells than in KO or KO/D508N cells (Fig. 2b).

Via flow cytometry, we observed that ATP13A2 promotes the cellular uptake of BODIPY-labelled polyamines[13]. WT-OE cells took up more BODIPY-SPD and BODIPY-SPM than D508N-OE or cells expressing firefly luciferase (Fluc, Extended Data Fig. 4a-b). Similarly, KO/WT cells presented a twofold higher BODIPY-SPM uptake than ATP13A2 KO and KO/D508N cells, which took up less than CON cells (Fig. 2c). The comparable FITC-dextran uptake in the KO/WT and KO/D508N cells (Extended Data Fig. 4c) demonstrated that the higher BODIPY-SPM uptake in KO/WT *versus* KO/D508N is not explained by an increased endocytic rate, but depends on ATP13A2's transport activity. The stimulatory effect of ATP13A2 on endocytosis appears as a transport-independent phenotype[14].

Since ATP13A2 transports SPM towards the cytosol (Fig. 1j) and increases the cellular SPM content (Fig. 2a-b), ATP13A2 may transport endocytosed polyamines into the cytosol. Indeed, endocytosis inhibitors prevented FITC-dextran uptake (Extended Data Fig. 4c) and blocked BODIPY-SPM uptake (Fig. 2c). Via confocal microscopy, we confirmed the higher cellular BODIPY-SPM content in KO/WT *versus* KO/D508N cells (Extended Data Fig. 1i). In the KO/D508N cells, BODIPY-SPM mainly co-localized with LAMP1 positive vesicles (Fig. 2d, Extended Data Fig. 1j-k), indicative for accumulation in the late endo-lysosomes, which is not a lysosomotropic effect[15]. In contrast, cells with functional ATP13A2 displayed a broader distribution of BODIPY-SPM, which was more abundant in the cytosol

and nucleus in agreement with the transport direction from lysosomal lumen to cytosol (Fig. 2d, Extended Data Fig. 1l). By stimulating cellular SPM uptake and transporting SPM into the cytosol, ATP13A2 complements endogenous SPM synthesis, which depends on the enzymes ornithine decarboxylase (ODC), SPD and SPM synthases. Indeed, KO/WT cells were protected against pharmacological inhibition of ODC or SPD/SPM synthase, while a lack of ATP13A2 activity sensitized KO and KO/D508N cells (Extended Data Fig. 4d-g), in line with the negative genetic interactions between ATP13A2 orthologues and ODC in yeast[16] and *Caenorhabditis elegans*[8].

Mutations disrupt ATP13A2 SPM activity

Via mutagenesis, we confirmed that SPM-dependent activation of ATP13A2 depends on residues in the predicted substrate binding site near transmembrane segment M4 (A467V on M4, D962N on M6 and K1062A on M8) (Fig. 2e, Extended Data Fig. 5a-b; rationale for residue choice in methods). Indeed, the three mutants displayed a lower SPM-induced ATPase activity and apparent SPM affinity (Fig. 2f), but also a reduced cellular uptake of BODIPY-SPD/SPM (Extended Data Fig. 5c, Fig. 2h) suggesting these residues contribute to SPM coordination in the membrane region. SPM-induced dephosphorylation is completely abolished in the D962N mutant (Fig. 2g, Extended Data Fig. 5d and 6) indicating that D962 may couple SPM binding to the dephosphorylation reaction.

Of the more than thirty identified disease-associated mutations in *ATP13A2* (Extended Data Fig. 7), we determined the activity of, mainly lysosomal localized, point mutants linked to EOPD or KRS. The KRS mutants T512I and G872R did not exhibit ATPase or auto-phosphorylation activity and were SPM-insensitive, in line with strongly reduced BODIPY-SPD/SPM uptake (Fig. 2i-l, Extended Data Fig. 5e-g). The effect of the EOPD mutations T12M, G528R and A741T was less severe. A reduction in the apparent SPM affinity was observed, phospho-enzyme levels were more (T12M) or less (G528R, A741T) sensitive to SPM, and BODIPY-SPD/SPM uptake in cells was more mildly impaired (Fig. 2i-l, Extended Data Fig. 5e-g). Together, all tested disease mutations disturb ATP13A2-dependent polyamine transport, and the degree of functional impact correlates with the EOPD *versus* KRS disease phenotype, although the mutation type is not the sole determinant of the clinical phenotype[17].

ATP13A2 protects against polyamine toxicity

We further investigated whether defective lysosomal polyamine export explains the lysosomal phenotype in ATP13A2 KO cells[3]. SPM and SPD are abundant organic polycations that support cell function, but at high concentrations, become toxic[18]. Indeed, high levels of SPM or SPD reduced the viability of CON cells after 24 h (Extended Data Fig. 8a-b), which was paralleled by an increased cell death (Fig. 3a), whereas ornithine and putrescine were not cytotoxic (Extended Data Fig. 8c-d). Importantly, loss of ATP13A2 activity exacerbated SPM/SPD toxicity (Fig. 3a, Extended Data Fig. 8a-b), which may be a direct consequence of lysosomal polyamine accumulation (Fig. 2d), leading to lysosomal dysfunction. Indeed, at a time point preceding cell death (4 h, Extended Data Fig. 8e), lysosomal acidification was compromised in KO and KO/D508N cells, which was aggravated upon SPM exposure (Fig. 3b). This pH neutralizing effect of SPM was absent in CON and KO/WT cells (Fig. 3b).

Lysosomal alkalization may explain the diminished lysosomal degradation potential (Fig. 3c) and cathepsin D (CTSD, Extended Data Fig. 8f) activity observed in KO and KO/D508N cells. Surprisingly, cathepsin B (CTSB) activity was elevated at toxic SPM levels (Fig. 3d) in line with its higher pH optimum, and most likely due to impaired lysosomal membrane integrity[19], which is a driver of lysosome-dependent cell death[20]. Indeed, we confirmed via an acridine orange (AO)-based assay that lysosomal membrane integrity in ATP13A2 KO and KO/D508N cells was impaired, which was more prominent following SPM challenge, a phenotype that was absent in CON and KO/WT cells (Fig. 3e). SPM treatment also increased the number and size of endogenous galectin 3 (Gal-3) punctae only in KO and KO/D508N cells, which is representative for lysosomal rupture (Fig. 3f). This was further confirmed by the loss of endo-lysosomal FITC-dextran punctae and a more diffuse, cytosolic CTSB staining in the KO and KO/D508N cells (Extended Data Fig. 8g-h). In line with reported findings[21], exposure to acidic nanoparticles restored lysosomal pH and functionality (Fig. 3b-c), prevented CTSB activation (Fig. 3d) and recovered lysosomal membrane intactness (Fig. 3e) ultimately reducing SPM-induced cell death (Fig. 3g). Moreover, pharmacological CTSB inhibition significantly reduced SPM toxicity in the KO and KO/D508N cells (Fig. 3h).

ATP13A2 protects in higher disease models

Lysosomal polyamine toxicity may be relevant in the context of neurodegeneration, since isolated mouse cortical neurons with miRNA-mediated Atp13a2 knockdown (Fig. 4a) were more susceptible to SPM-induced cell death than control neurons (miR-Fluc, miRNA targeted to Fluc) (Fig. 4b). Interestingly, increased SPM sensitivity of neurons with Atp13a2 knockdown was attenuated either by inhibition of CTSB (Extended Data Fig. 9); or by rescue with human ATP13A2 WT, but not the D508N mutant (Fig. 4b).

Finally, SPD exposure hampered growth capacity in *C. elegans* N2 (wild-type) animals, which was marked by developmental delay and, hence, reduced worm length. This was exacerbated in animals with deficiency in ATP13A2 orthologues (*catp-5(0)*, *catp-6(0)* or *catp-7(0)*[22]) (Fig. 4c). The phenotype of CATP-6- and CATP-7-deficient strains was rescued by CATP-6 or CATP-7 WT, but not a catalytically dead variant, showing that the transport activity is required (Fig. 4c).

Discussion

Polyamines are physiologically important polycations that are tightly regulated by a complex interplay of import, export, synthesis and degradation[18]. As a polyamine transporter that controls the cellular polyamine content, ATP13A2 emerges as a member of the elusive mammalian polyamine transport system[18]. Extracellular polyamines most likely bind to plasma membrane heparan sulphate proteoglycans[23] and enter the cell via endocytosis[24] prior to transport into the cytosol by ATP13A2 (Fig. 4d). Also the other P5B-ATPases ATP13A3-5 residing in the endosomal system, share high sequence similarity in the substrate binding region[12], and may belong to the mammalian polyamine transport system.

Genetic insights point to a major role of lysosomal dysfunction in PD, contributing to α-synuclein aggregation and mitochondrial dysfunction[25]. Here, we demonstrate that impaired lysosomal polyamine export represents a novel lysosome-dependent cell death pathway that may be implicated in ATP13A2-associated neurodegeneration. In addition, defective ATP13A2 diminishes cellular polyamines, which

may potentiate the disease phenotype, since polyamines are scavengers of reactive oxygen species[26], heavy metals, and regulate autophagy[27]. The dual impact of ATP13A2 on both lysosomal and cytosolic polyamine levels may explain the broad phenotype associated with ATP13A2 loss of function[5]. Other PD related genes may also impact on ATP13A2 functionality or may be affected by disturbed polyamine homeostasis. Polyamine levels decline with age, whereas polyamine supplementation increases life span in several model organisms[27]. Conversely, defective SPM synthase causes Snyder-Robinson syndrome, a form of X-linked intellectual disability[28], and reduced SPD/SPM N1-acetyltransferase 1 (SAT1) expression has been implicated in PD[29]. Modulation of polyamine homeostasis may therefore be considered for neuroprotective therapy.

In conclusion, ATP13A2 dysfunction prevents late endo-lysosomal polyamine export and sensitizes cells to lysosomal disruption by exogenous polyamines.

Online content

Methods, extended data, supplementary information and accompanying references; acknowledgements; Nature Research reporting summaries; peer review information; details of author contributions and competing interests; and statements of data availability are available at XXXXXX.

Main References

1 Ramirez, A. *et al.* Hereditary parkinsonism with dementia is caused by mutations in ATP13A2, encoding a lysosomal type 5 P-type ATPase. *Nature genetics* **38**, 1184-1191, doi:10.1038/ng1884 (2006).

2 Di Fonzo, A. *et al.* ATP13A2 missense mutations in juvenile parkinsonism and young onset Parkinson disease. *Neurology* **68**, 1557-1562, doi:10.1212/01.wnl.0000260963.08711.08 (2007).

3 Dehay, B. *et al.* Loss of P-type ATPase ATP13A2/PARK9 function induces general lysosomal deficiency and leads to Parkinson disease neurodegeneration. *Proc Natl Acad Sci U S A* **109**, 9611-9616, doi:10.1073/pnas.1112368109 (2012).

4 Palmgren, M. G. & Nissen, P. P-type ATPases. *Annual review of biophysics* **40**, 243-266, doi:10.1146/annurev.biophys.093008.131331 (2011).

5 van Veen, S. *et al.* Cellular function and pathological role of ATP13A2 and related P-type transport ATPases in Parkinson's disease and other neurological disorders. *Frontiers in molecular neuroscience* **7**, 48, doi:10.3389/fnmol.2014.00048 (2014).

6 Narayanaswamy, N. *et al.* A pH-correctable, DNA-based fluorescent reporter for organellar calcium. *Nat Methods*, doi:10.1038/s41592-018-0232-7 (2018).

7 De La Hera, D. P., Corradi, G. R., Adamo, H. P. & De Tezanos Pinto, F. Parkinson's disease-associated human P5B-ATPase ATP13A2 increases spermidine uptake. *Biochem J* **450**, 47-53, doi:10.1042/BJ20120739 (2013).
8 Heinick, A. *et al.* Caenorhabditis elegans P5B-type ATPase CATP-5 operates in polyamine transport and is crucial for norspermidine-mediated suppression of RNA interference. *FASEB J* **24**, 206-217, doi:10.1096/fj.09-135889 (2010).
9 Holemans, T. *et al.* A lipid switch unlocks Parkinson's disease-associated ATP13A2. *Proc Natl Acad Sci U S A* **112**, 9040-9045, doi:10.1073/pnas.1508220112 1121508220112 [pii] (2015).
10 Martin, S., Holemans, T. & Vangheluwe, P. Unlocking ATP13A2/PARK9 activity. *Cell Cycle* **14**, 3341-3342, doi:10.1080/15384101.2015.1093420 (2015).
11 Martin, S. *et al.* Protection against Mitochondrial and Metal Toxicity Depends on Functional Lipid Binding Sites in ATP13A2. *Parkinson's disease* **2016**, 9531917, doi:10.1155/2016/9531917 (2016).
12 Sorensen, D. M. *et al.* Parkinson disease related ATP13A2 evolved early in animal evolution. *PLoS One* **13**, e0193228, doi:10.1371/journal.pone.0193228 (2018).
13 Vanhoutte, R., Kahler, J. P., Martin, S., van Veen, S. & Verhelst, S. H. L. Clickable Polyamine Derivatives as Chemical Probes for the Polyamine Transport System. *Chembiochem* **19**, 907-911, doi:10.1002/cbic.201800043 (2018).
14 Demirsoy, S. *et al.* ATP13A2/PARK9 regulates endo-/lysosomal cargo sorting and proteostasis through a novel PI(3, 5)P2-mediated scaffolding function. *Hum Mol Genet* **26**, 1656-1669, doi:10.1093/hmg/ddx070 (2017).
15 Seglen, P. O. & Gordon, P. B. Effects of lysosomotropic monoamines, diamines, amino alcohols, and other amino compounds on protein degradation and protein synthesis in isolated rat hepatocytes. *Mol Pharmacol* **18**, 468-475 (1980).
16 Chatr-Aryamontri, A. *et al.* The BioGRID interaction database: 2017 update. *Nucleic Acids Res* **45**, D369-D379, doi:10.1093/nar/gkw1102 (2017).
17 Estrada-Cuzcano, A. *et al.* Loss-of-function mutations in the ATP13A2/PARK9 gene cause complicated hereditary spastic paraplegia (SPG78). *Brain* **140**, 287-305, doi:10.1093/brain/aww307 (2017).
18 Pegg, A. E. Functions of Polyamines in Mammals. *J Biol Chem* **291**, 14904-14912, doi:10.1074/jbc.R116.731661 (2016).
19 Qiao, C. *et al.* Atp13a2 Deficiency Aggravates Astrocyte-Mediated Neuroinflammation via NLRP3 Inflammasome Activation. *CNS Neurosci Ther* **22**, 451-460, doi:10.1111/cns.12514 (2016).
20 Aits, S. & Jaattela, M. Lysosomal cell death at a glance. *Journal of cell science* **126**, 1905-1912, doi:10.1242/jcs.091181 (2013).
21 Bourdenx, M. *et al.* Nanoparticles restore lysosomal acidification defects: Implications for Parkinson and other lysosomal-related diseases. *Autophagy* **12**, 472-483, doi:10.1080/15548627.2015.1136769 (2016).
22 Zielich, J. *et al.* Overlapping expression patterns and functions of three paralogous P5B ATPases in Caenorhabditis elegans. *PLoS One* **13**, e0194451, doi:10.1371/journal.pone.0194451 (2018).
23 Belting, M. *et al.* Glypican-1 is a vehicle for polyamine uptake in mammalian cells: a pivital role for nitrosothiol-derived nitric oxide. *J Biol Chem* **278**, 47181-47189, doi:10.1074/jbc.M308325200 (2003).
24 Uemura, T., Stringer, D. E., Blohm-Mangone, K. A. & Gerner, E. W. Polyamine transport is mediated by both endocytic and solute carrier transport mechanisms in the gastrointestinal tract. *Am J Physiol Gastrointest Liver Physiol* **299**, G517-522, doi:10.1152/ajpgi.00169.2010 (2010).
25 Klein, C. & Westenberger, A. Genetics of Parkinson's disease. *Cold Spring Harb Perspect Med* **2**, a008888, doi:10.1101/cshperspect.a008888 (2012).
26 Ha, H. C. *et al.* The natural polyamine spermine functions directly as a free radical scavenger. *Proc Natl Acad Sci U S A* **95**, 11140-11145 (1998).

27 Madeo, F., Eisenberg, T., Pietrocola, F. & Kroemer, G. Spermidine in health and disease. *Science* **359**, doi:10.1126/science.aan2788 (2018).
28 Li, C. *et al.* Spermine synthase deficiency causes lysosomal dysfunction and oxidative stress in models of Snyder-Robinson syndrome. *Nat Commun* **8**, 1257, doi:10.1038/s41467-017-01289-7 (2017).
29 Lewandowski, N. M. *et al.* Polyamine pathway contributes to the pathogenesis of Parkinson disease. *Proc Natl Acad Sci U S A* **107**, 16970-16975, doi:10.1073/pnas.1011751107 (2010).
30 Sorensen, D. M., Buch-Pedersen, M. J. & Palmgren, M. G. Structural divergence between the two subgroups of P5 ATPases. *Biochim Biophys Acta* **1797**, 846-855, doi:10.1016/j.bbabio.2010.04.010 (2010).

Figure legends

Figure 1 – ATP13A2 is a polyamine transporter. (a) Chemical structures of ornithine (ORN), putrescine (PUT), spermidine (SPD) and spermine (SPM). (**b-d)** Measurements on solubilized SH-SY5Y microsomes overexpressing ATP13A2 WT-OE. **(b)** Dose-response curves of SPM, SPD, PUT and ORN on ATP13A2 ATPase activity. **(c)** Phospho-enzyme (EP) levels of WT-OE in the presence of increasing SPM concentrations. Upper panel: representative autoradiogram; lower panel: EP quantification. **(d)** WT-OE microsomes pulse ([γ-^{32}P] ATP) chase (cold ATP) of dephosphorylation +/- 1 mM SPM. **(e)** ATPase activity of purified ATP13A2 under increasing concentrations of SPM (+/- PA and/or PI(3,5)P2). **(f)** Dose-response curves of SPM, SPD and PUT on purified ATP13A2 ATPase activity supplemented with PA and PI(3,5)P2 (as a reference, SPM + PA/PI(3,5)P2 from **e**). **(g)** Purified ATP13A2 (WT or E343A mutant) pulse ([γ-^{32}P] ATP) chase (cold ATP) of dephosphorylation measured +/- 1 mM SPM. **(h)** Illustration of vesicle reconstitution and the ^{3}H-spermine (^{3}H-SPM) transport assay. **(i)** Immunoblot of reconstituted vesicles. **(j)** Uptake of ^{3}H-SPM in reconstituted vesicles derived from yeast overexpressing BAD-tagged ATP13A2 (WT or E343A mutant) supplemented with phosphatidylcholine and PA, +/- intraluminal ATP and an ATP-regenerating system. Data are presented as mean ± S.E.M. (**b-g**) or box and whisker plots with overlaid individual data points representing replicates (**j**, horizontal line = median, 25/75 percentiles). Values of N (independent biological experiments) were N = 3: **b** (ORN, SPD), **d-g** (E343A), **i**, **j** (WT ATP outside; E343A); N = 4: **c**, **e** (no lipid); N = 5: **b** (PUT), **g** (WT); N = 6: **j** (WT no ATP), **b** (SPM); N = 8: **j** (WT ATP inside). Analysis by two-way ANOVA with Tukey's (**g**) or one-way ANOVA with Tukey's (**j**). Fitted lines: nonlinear

allosteric sigmoidal (**b**, **e-f**) or two phase decay (**c**, **d**, **g**). For gel source data, see Supplementary Figure 1.

Figure 2 – ATP13A2 transport affects cellular polyamine uptake, which is impaired by catalytic and disease mutations. (a-b) Metabolomics of cellular polyamines in ATP13A2 KO (KO) *vs.* SH-SY5Y controls (CON) **(a)**, or *vs.* rescue cell lines with expression of ATP13A2 WT (KO/WT) or D508N (KO/D508N) **(b)**. **(c)** BODIPY-SPM uptake +/- endocytosis inhibitors (Dynasore, Genistein and/or Pitstop 2), alone or in combination (combo). (**d**) Confocal microscopy of BODIPY-SPM distribution (as described in methods). Scale bar = 5 µm. Arrow represents expanded region in upper panels, dashed line analysed in Extended data Fig. 1j. Immunoblotting **(e)** and SPM-induced ATPase activity **(f)** of microsomes expressing ATP13A2 WT, D508N or catalytic mutants in M4 (A467V), M6 (D962N), and M8 (K1062A)[30]. **(g)** Representative autoradiogram of ATP13A2 WT *vs.* mutant auto-phosphorylation (EP) +/- 1 mM SPM. **(h)** Cellular BODIPY-SPM uptake in the indicated cell lines. Immunoblotting **(i)** or SPM-induced ATPase activity **(j)** of SH-SY5Y microsomes overexpressing disease associated mutants (Kufor-Rakeb syndrome (T512I and G872R) or early-onset Parkinson's disease (T12M, G528R, A741T)). SPM dose-response curve from Fig. 1b is shown as reference in **(f)** and **(j)**. **(k)** Representative autoradiogram of ATP13A2 WT *vs.* disease mutant auto-phosphorylation (EP) +/- 1 mM SPM. **(l)** BODIPY-SPM uptake in indicated cell lines. MFI, mean fluorescence intensities; (-), vehicle treated sample. Data are presented as individual data points (representing replicates) overlaid on box and whisker plots (**a-b**, horizontal line = median, 25/75 percentiles) or mean (**c**, **h**, **l**), or mean ± S.E.M. (**f**, **j**). The values of N (independent biological experiments) were N = 3: **d-f**, **g** (D508N, A467V, D962N, K1062A (SPM)), **h**, **j** (T12M, T512I, G872R), **k** (T12M (-), T12M, T512I, G528R, A741T, G872R (SPM)), **l**; N = 4: **a-c** (KO, KO/WT, KO/DN), **g** (D508N, A467V, D962N, K1062A (-)), **i**, **j** (A741T, G528R), **k** (WT, T512I, G528R, A741T, G872R (-)); N = 5: **c** (CON), **g** (WT (-)); N = 6: **g** (WT (SPM)), **k** (WT (SPM)). Analysis by one-way ANOVA with Tukey's (**a-c**) or Dunnett's (**h-l**). Fitted lines: nonlinear allosteric sigmoidal (**f** (D962N, D508N), **j**) or one-phase association (**f** (A467V, K1062A)). For gel source data see Supplementary Figure 1.

Figure 3 – ATP13A2 protects against lysosome-dependent SPM toxicity. (a) SPM-induced cell death (PI, propidium iodide) in SH-SY5Y control (CON), ATP13A2 KO (KO) and rescue cell lines with WT (KO/WT) or D508N (KO/D508N). **(b-f)** Impact of SPM (10 µM, 4 h) and acidic nanoparticles (NP, 100 nm diameter; Extended Data Fig. 8j) on lysosomal functionality. **(b)** Lysosomal pH measured by ratiometric FITC-dextran (standard curve, Extended Data Fig. 8i). **(c-d)** Lysosomal degradation capacity analysed by **(c)** DQ-BSA or **(d)** cathepsin B (CTSB) activity. **(e-f)** Assessment of lysosomal membrane integrity via acridine orange (AO) staining **(e)**, or galectin-3 (Gal-3) punctae formation (lysosomal rupture) **(f)**. Confocal images depict representative images (DAPI staining for nuclei reference, scale bar, 2.5 µm). The box and whisker plots depict the size (left) and number (right) of punctae. **(g-h)** The effect of NP **(g)** or the CTSB inhibitor CA-074 **(h)** (25 µM) on SPM-induced cytotoxicity. MFI, mean fluorescence intensities. (-), vehicle treated sample. Data are presented as individual data points (representing replicates) overlaid on box and whisker plots (**b-f,** horizontal line = median, 25/75 percentiles) or means (**g-h**), or the mean ± S.E.M. (**a**). The values of N (independent biological experiments) were N = 3: **a**, **b-d** (NP, NP + SPM), **f-h**; N=4: **e**, (NP, NP + SPM), N = 6: **b-d** ((-), SPM), N = 7: **e** ((-), SPM). Analysis by two-way ANOVA with Dunnett's test (**a**); one-way ANOVA with Tukey's (**b-e**, **g-h**) or Sidak's test (**f**). Fitted lines: nonlinear log(inhibitor) *vs.* response (variable slope) (**a**).

Figure 4 – Loss of ATP13A2 orthologues exacerbates polyamine toxicity in primary neurons and *C. elegans*. (a) Lentiviral knockdown of Atp13a2 in isolated murine cortical neurons (miR-3 or miR-5) was confirmed by qRT-PCR relative to Gapdh. miR-Fluc (miRNA against Firefly luciferase), negative control. **(b)** miR-Fluc and Atp13a2 knockdown neurons were transduced with Fluc, human ATP13A2 WT or D508N. SPM-induced cytotoxicity was assayed via TUNEL staining. Left, representative confocal images; right, box and whiskers plot depicting TUNEL positivity. **(c)** The indicated worm strains were assessed for SPD toxicity. Worm lengths were determined as a read-out for toxicity. Scale bar = 100 µm. Top: quantification; bottom: representative images. **(d)** Illustration of the proposed mechanism of endo-lysosomal polyamine uptake and transfer into the cytosol via ATP13A2. (-), vehicle treated. Data are presented as mean (**a**) or as box and whisker plots (**b-c**, horizontal line = median, 25/75

percentiles) with individual data points representing replicates. The values of N (independent biological experiments) were N = 2: (**a**), N = 3: **(b-c)**. Analysis by one-way ANOVA with Tukey's (**b-c**).

Methods

Materials – The following reagents were purchased from Sigma-Aldrich: sodium orthovanadate (S6508), $CaCl_2$ (C3881), $ZnCl_2$ (Z0152), $MnCl_2$ (M3634), $FeCl_3$ (157740), SPM (S3256), SPD (S2626), N^1-acetylspermine trihydrochloride (01467), N^1-acetylspermidine hydrochloride (9001535-1), N^8-acetylspermidine dihydrochloride (A3658), putrescine dihydrochloride (P7505), L-arginine (A5006), L-ornithine monohydrochloride (O2375), histamine (H7250), agmatine sulfate salt (A7127), dopamine hydrochloride (H8502), cadaverine (D22606), yeast nitrogen base without amino acids (Y0626), yeast drop-out mix without uracil (Y1501), glucose (G8720), streptavidin sepharose (GE17-5113-01), thrombin (GE27-0846-01), DMSO (276855), DFMO (D193), Dynasore (D7693), Pitstop 2 (SML1169), 4-methylumbelliferyl heptanoate (MUH, M2514), PI (P4170), CA-074 (C5732), fluorescein isothiocyanate-dextran (FITC-dextran, 46945), DAPI (D9542), anti-ATP13A2 antibody (A3361), anti-GAPDH antibody (G8795), Resomer® RG 503H (719870) and SigmaFast protease inhibitor (S8820). In addition, 18:1 PI(3,5)P2 [1,2-dioleoyl-sn-glycero-3-phospho-(1'-myo-inositol-3',5'-bisphosphate) (ammonium salt); 850154], 18:1 PA [1,2-dioleoyl-sn-glycero-3-phosphate (sodium salt); 840875] and egg phosphatidylcholine (840051) were obtained from Avanti Polar Lipids. Bovine serum albumin (BSA; 3854.3) was obtained from Carl Roth. Yeast extract (103753.0500) was purchased from VWR, and n-dodecyl-β-D-maltopyranoside (DDM; 1758-1350) was purchased from Inalco. We obtained Bio-Beads SM-2 resin (1523920) from Bio-Rad. ^{3}H-SPM (ART 0471) was ordered from ARC. APCHA (sc-202715) and 4MCHA (sc-272662) were purchased from Santa Cruz Biotechnology. Genistein (ab120112), anti-galectin-3 antibody (ab2785), anti-LAMP1 antibody (Abcam, ab24170) and anti-cathepsin B antibody (ab58802) were purchased from Abcam. TRYPLE (12604021), AO (A1372) and DQ-Green BSA (D12050) were ordered from Life Technologies.

Compound/inhibitor preparation – All polyamines, diamines, monoamines and amino acids were prepared to a final stock concentration of 500 mM (200 mM in the case of SPM) in 0.1 M MOPS-KOH

(pH 7.0). DFMO was prepared to a final stock concentration of 500 mM in mQ H_2O. The inhibitors 4MCHA and APCHA were dissolved in DMSO to a final stock concentration of 200 mM. The endocytosis inhibitors Dynasore, genistein and Pitstop 2 were dissolved in DMSO to final concentrations of 50 mM, 25 mM and 25 mM, respectively. The cathepsin B inhibitor CA-074 was dissolved in DMSO to a final concentration of 25 mM.

Generation of SH-SY5Y cell models – SH-SY5Y human neuroblastoma cells were transduced with lentiviral vectors to obtain stable overexpression of firefly luciferase (Fluc) or human ATP13A2 (isoform 2, WT (ID: NP_001135445), indicated disease or catalytic mutants) and maintained as described previously[9-11]. Catalytic mutants; A467V on M4, D962N on M6 and K1062A on M8 were generated by mutagenesis. P5 type ATPases were discovered by genome sequence analysis 20 years ago and contain highly conserved motifs for function and substrate binding[31]. The A467V mutation converts PPALP of the predicted substrate binding site in transmembrane segment M4 into PPVLP that is present in ATP13A5[4,30]. Also neighbouring membrane helices contribute to substrate coordination in P-type ATPases, which often relies on conserved and charged residues, such as D962 in M6 and K1062 in M8 of ATP13A2[4]). Furthermore, mutants associated with Kufor-Rakeb syndrome (T512I[3,32,33] and G872R[34]) or early-onset Parkinson's disease (T12M[2], G528R[2], and A741T[35-37]) were generated. All cell lines were produced at varying viral vector titres and assessed for equal expression to ATP13A2 WT.

For CRISPR/Cas9-mediated KO of ATP13A2, the lentiviral vector lentiCRISPRv2 (Addgene: #52961)[38] was used. First, the Cas9 cassette was transformed into a high-fidelity Cas9 (Cas9-HF) by Gibson assembly with a gBlock gene fragment (Integrated DNA Technologies) of the Cas9 portion encoding a protein product with HF mutations (N497A/R661A/Q695A/Q926A). This Cas9 variant triggers less off-target events while retaining its on-target activity[39]. A single-guide RNA (sgRNA) targeted to Atp13a2 was designed taking into account a high on-target efficiency, using sgRNA Designer (https://portals.broadinstitute.org/gpp/public/analysis-tools/sgrna-design)[40], and a low off-target efficiency, via CRISPR Design (http://crispr.mit.edu/). A lentiviral CRISPR/Cas9 HF expression plasmid was created by inserting fragments that contained an sgRNA sequence of ATP13A2 (F: 5'-CACCGGTCAGGGTCCCATAACCGGT; R: 5'-AAACACCGGTTATGGGACCCTGACC) into the

lentiCRISPRv2 vector. The generated CRISPR-Cas9 HF-ATP13A2 plasmid (1,000 ng), the packaging plasmid pCMV-ΔR8.91 (900 ng), and the envelope plasmid pMD2G-VSV-G (Addgene, 12259) (100 ng) were mixed together with 200 µl of JetPrime buffer and 4 µl of JetPrime reagent (Polyplus-transfection) for transfection of HEK-293T cells according to the manufacturer's protocol. After 4 hours (h) at 37°C and 5% CO_2, the serum-free medium was replaced with DMEM/F12 (Dulbecco's modified Eagle's medium, Nutrient Mixture F-12) supplemented with 10% fetal calf serum (heat-inactivated). 48 h later, the lentiviral vectors were collected by passing the medium through a 0.45 µm filter, and 0.5 ml of this medium was used to transduce SH-SY5Y cells supplemented with 8 µg/ml polybrene (Sigma-Aldrich). 24 h after transduction, cells were selected in 3 µg/ml puromycin (Sigma-Aldrich) and passaged three times before single clones were isolated via serial dilution. The resulting cells were examined by qRT-PCR (F: 5'-ACCGGTTATGGGACCCTGAC; R: 5'-GTGATAGCCGATGACCCTCC) and Western blotting. For rescue experiments, ATP13A2 KO cells were stably transduced with lentiviral vectors expressing ATP13A2 WT or D508N mutant in which both cDNAs were modified with synonymous mutations at the sgRNA target site. All cell lines were routinely assessed for mycoplasma and cultured for a maximum of 20 passages.

Membrane fractionation – SH-SY5Y cells were seeded in 15 cm dishes at a density of 6 x 10^6 cells per plate. 24 h later, the cells were harvested following trypsinization and brief centrifugation (300 x g, 5 min). Subcellular fractionation was performed by differential centrifugation, as described previously[9-11]. The microsomal protein concentration was measured using the bicinchoninic acid assay (Thermo Fischer Scientific, Pierce) according to the manufacturer's instructions.

ATPase assay – The ATPase activity of ATP13A2 was assessed using a commercially available luminescence assay (ADP-Glo Max assay, Promega) that monitors the production of ADP via luciferase activity. Substrate screen was designed to include candidates previously postulated in the literature[6-8,41-45]. The reactions were performed for 30 min (37°C) in a final volume of 25 µl. The assay reaction mixture contained 50 mM MOPS-KOH (pH 7), 100 mM KCl, 11 mM $MgCl_2$, 1 mM DTT, 195 µM DDM, various concentrations of the indicated compound, and either microsomes (5 µg) harvested from SH-SY5Y cells overexpressing ATP13A2 (WT or mutants) or purified ATP13A2 (0.3-0.5 µg). When

purified ATP13A2 was used, we included 125 µM PA, 125 µM PI(3,5)P_2 and 19.5 µM DDM in the reaction buffer. The assay was started by the addition of 5 mM ATP and was terminated by adding 25 µl of ADP-Glo Reagent. The 96-well plate was then incubated for 40 min at room temperature, followed by the addition of 50 µl of ADP-Glo Max Detection Reagent. After 40 min, luminescence was detected using a FlexStation 3.0 system (Molecular Devices). Dose-response curves and $n/K_m/V_{max}$ values were calculated using GraphPad Prism Software (GraphPad Software Inc.).

Auto-phosphorylation assay – The auto-phosphorylation activity of ATP13A2 on the conserved D508 residue was measured as described previously[9,12,17]. Briefly, microsomes (20 µg) or purified ATP13A2 (1 µg) were incubated with radioactively labelled ATP in the presence of the indicated SPM or ornithine concentrations, and after 1 min, the reaction was stopped. In case of purified ATP13A2, 125 µM PA and 125 µM PI(3,5)P2 were included in the reaction mixture. To determine the sensitivity of the ATP13A2 phospho-enzyme to ATP or a combination of ATP and SPM, 30 s after adding ^{32}P-ATP, samples were incubated with non-radioactive ATP (5 mM in experiments using microsomes, 1 mM when purified ATP13A2) and SPM (1 mM) before the reaction was stopped at the indicated time points. The incorporation of ^{32}P was visualized following SDS-PAGE under acidic conditions and subsequently detected by autoradiography (microsomes) or liquid scintillation counting (purified ATP13A2) (Liquid Scintillation Analyzer TRI-CARB 2900TR).

Transformation and overexpression of ATP13A2 in yeast – The *S. cerevisiae* W303-1B/Gal4-ΔPep4 strain (leu2-3, his3-11,15, trp1-1::TRP1-GAL10-GAL4, ura3-1, ade2-1, canr, cir$^+$, ΔPep4 MAT; a kind gift from Rosa Lopez Marques) was transformed according to the lithium acetate/single-stranded carrier DNA/polyethylene glycol method[46], with the pYeDP60 vector containing a yeast codon optimized version of human *ATP13A2* variant 2 (WT or the catalytically dead E343A mutant) followed by a thrombin cleavage site and a C-terminal Biotin Acceptor Domain (BAD) tag[47,48]. The transformation mixture was grown for 48 h at 30°C on minimal medium agar plates lacking uracil (0.54% yeast nitrogen base without amino acids, 0.12% yeast drop-out mix without Ura, 2% glucose, and 2% agar) to select yeast colonies that acquired the plasmid. These colonies were then cultured in 20 ml of MM-Ura medium (0.67% yeast nitrogen base without amino acids, 0.19% yeast drop-out mix without Ura, and 2%

glucose) and grown for 24 h at 28°C and 200 rpm. The MM-Ura yeast pre-culture was used to inoculate 100 ml of MM-Ura medium to a final OD_{600} of 0.2, followed by a 12 h incubation period (28°C and 200 rpm). The second pre-culture was inoculated into 4.5 l of YPGE2X medium (2% yeast extract, 2% bactopeptone, 1% glucose, and 2.7% ethanol) to a final OD_{600} of 0.05 and grown for 36 h (28°C and 175 rpm). ATP13A2-BAD expression was induced with 2% galactose, followed by a second galactose induction 12 h later. After another 12 h, the pellet was collected (1,000 x g; 10 min; 4°C).

Yeast membrane preparation – Yeast cells were broken with glass beads using a BeadBeater (BioSpec products). The lysis buffer contained 50 mM Tris-HCl (pH 7.5), 1 mM EDTA, 0.6 M sorbitol, 1 mM phenylmethylsulfonyl fluoride and SigmaFast protease inhibitor. To remove cell debris and nuclei, the crude extract was centrifuged at 2,000 x g for 20 min (4°C). The supernatant (S1) was centrifuged at 20,000 x g for 20 min (4°C) to pellet the heavy membrane fraction (P2), and the resulting supernatant (S2) was further centrifuged at 200,000 x g for 1 h (4°C). The resulting pellet (*i.e.,* the light membrane fraction, P3) was resuspended in 20 mM HEPES-Tris (pH 7.4), 0.3 M sucrose and 0.1 mM $CaCl_2$. The total protein concentration was determined using a Bradford assay (B6916, Sigma-Aldrich).

ATP13A2-BAD purification – The method used to purify ATP13A2 was based on the purification of overexpressed Drs2p from yeast membranes[47]. Yeast P3 membranes were diluted to 5 mg of total protein/ml in SSR buffer (50 mM MOPS-KOH (pH 7), 100 mM KCl, 20% glycerol, 5 mM $MgCl_2$, 1 mM DTT, and SigmaFast protease inhibitor cocktail) and solubilized using DDM, with a detergent to protein ratio of 1:1. The samples were stirred on ice for 30 min, followed by centrifugation (100,000 x g; 1 h; 4°C) to pellet non-solubilized membranes. The solubilized material was incubated with streptavidin beads for 4 h (4°C) to allow binding of BAD-tagged ATP13A2 to the resin. To eliminate unbound material, the resin was washed four times with three resin volumes of SSR buffer supplemented with 0.5 mg/ml DDM. Subsequent cleavage by thrombin (0.0625 U/mg total protein) allowed the release of ATP13A2 from the beads by overnight incubation at 4°C. Finally, a Vivaspin Turbo 4 concentrator (100 kDa MWCO, Sartorius) was used to concentrate the sample. The protein concentration was determined using a Bradford assay. The quality of the purification was evaluated via SDS-PAGE followed by Coomassie staining or immunoblotting, as described previously[9-11]. Furthermore, the

purified ATP13A2 sample was analyzed by linear mode MALDI-TOF MS (Applied Biosystems 4800 Proteomics Analyzer) in the presence of α-Cyano-4-hydroxycinnamic acid as matrix and after C4 omix (Agilent) pipette tip purification.

Reconstitution of yeast membranes – To reconstitute yeast membranes, we followed a similar strategy as described before[49]. P3 membranes from the yeast membrane preparation expressing the ATP13A2-BAD construct were solubilized in buffer T (10 mM Tris-HCl (pH 7.4) and 1 mM EDTA) supplemented with 1.4% DDM. After removing the insoluble fraction by ultracentrifugation (30 min; 200,000 x g), the detergent extract was supplemented with 4.5 mM egg phosphatidylcholine and 0.5 mM 18:1 PA (in buffer T containing 0.7% DDM). The extract was then treated with Bio-Beads to remove the DDM and reconstitute proteoliposomes (*i.e.,* "no ATP inside" condition). To generate proteoliposomes that contained intraluminal ATP (*i.e.,* "ATP inside" condition), we added 5 mM ATP and an ATP-regenerating system before incubation with the Bio-Beads. Finally, the vesicles were recovered by ultracentrifugation (1 h; 200,000 x g) and resuspended in buffer T. The protein concentration was determined using a Bradford assay.

Transport assay using reconstituted vesicles – ^{3}H-SPM uptake into freshly prepared vesicles was measured within 60 min. The above-described vesicles ("no ATP inside" or "ATP inside") were diluted to 1 µg/µl in buffer T. The reactions were performed for 10 min (30°C) in a final volume of 1 ml. The assay reaction mixture contained 50 mM MOPS, 100 mM KCl, 11 mM $MgCl_2$, 1 mM DTT and reconstituted vesicles (45 µg). The reaction was started by adding 1 mM ^{3}H-SPM. For the condition "no ATP inside", 5 mM ATP and an ATP-regenerating system were added after Bio-Bead treatment, prior to the addition of ^{3}H-SPM. The reaction was stopped by filtering the samples through Millipore filters (0.45 µm). Following washing of the filters with assay buffer, radioactivity retained on the filters was counted using a liquid scintillation counter (Liquid Scintillation Analyzer TRI-CARB 2900TR).

Cellular transport assay and endocytosis assessment – BODIPY-SPD and BODIPY-SPM were synthesized as described previously (compounds 14 and 15, respectively)[13]. The cells were seeded in 12-well plates (1.0 X 10^5 cells per well) and the next day, the cells were incubated with 5 µM BODIPY-SPM or BODIPY-SPD for 2 h before harvesting. To assess endocytosis, the cells were pre-treated (30

min) with the endocytosis inhibitors Dynasore (100 µM), genistein (50 µM) and/or Pitstop 2 (50 µM) prior to the addition of either 20 µg/ml FITC-dextran or BODIPY-SPM (2 h and 37°C). The cells were then collected (300 x g, 5 min), washed and resuspended in PBS containing 1% BSA. Finally, an Attune Nxt (Thermo Fischer Scientific) flow cytometer was used to record the mean fluorescence intensities (MFI) of 10,000 events per treatment.

Metabolomics – Cells were grown into a 6-well plate and extracted as described previously[50]. Briefly, the medium was removed and cells were washed with a 0.9% NaCl solution. The washing solution was removed and 150 µl of a 6% trichloroacetic acid (TCA, Sigma) was added for the extraction. Using a cell scraper, the full extract was transferred into an eppendorf and incubated for 30 min on ice. Insolubilities such as precipitated proteins were removed by centrifugation for 20 min at 20,000 x g at 4°C. To 100 µl of the supernatant, 900 µl of a 100 mM sodium carbonate buffer (pH 9.0) was added. Next, 25 µl of isobutyl chloroformate (Sigma) was added and the mixture was incubated for 30 min at 35°C. 800 µl of the reaction mixture was transferred to a 2 ml eppendorf tube and 1 ml of diethylether (Sigma) was added. The mixture was vortexed vigorously and placed for 15 min at 25°C. 900 µl of the upper phase was transferred into an eppendorf and dried using a vacuum centrifuge. Finally, the dried extract was dissolved in 125 µl of a 50% acetonitrile (LC-MS grade, Merck) solution in water containing 0.2% acetic acid. Medium samples were extracted by adding 100 µl of 4% TCA to 100 µl of medium. The subsequent modifications were similar as described above.

15 µl of the extract was loaded onto a Thermo Scientific Liquid Chromatography QQQ (Quantiva, Thermo Scientific) equipped with an ACQUITY UPLC BEH C18 (1.7 µm, 2.1 x 100 mm) column from WATERS. Solvent A consisted of ultrapure H_2O with 0.2% acetic acid while solvent B was acetonitrile (Merck) with 0.2% acetic acid; all solvents used were LC-MS grade. Flow rate remained constant at 250 µl/min, and the column temperature remained constant at 30°C. A gradient for the separation of modified polyamines was applied as follows: from 0 to 2 min 20% B, from 2 to 10 min a linear increase to 85% B was carried out and remained at 85% B until 17 min. At 18 min the gradient returned to 20% B. The method stopped at 22 min. The MS operated in positive ion mode (3500 V); the source settings were as follows: Sheath gas at 50, Aux Gas at 10. Ion Transfer tube was heated at 325°C and Vaporizer

temperature was set at 350°C. The MS operated in MRM mode and used the following transitions: ornithine (parent m/z at 333.2 --> fragment 315.2, collision energy at 10.25V), putrescine (parent m/z at 289.2 --> fragment 215.2, collision energy at 10.25V), SPD (parent m/z at 446.4 --> fragment 198.2, collision energy at 23.6V) and SPM (parent m/z at 603.4 --> fragment 455.1, collision energy at 19.91V). Peak area was integrated using the XCalibur Quan tool (version 4.2.28.14, Thermo Scientific).

Preparation and characterization of acidic nanoparticles – Acidic nanoparticles were prepared as previously described[21]. Briefly, 31 mg of Resomer® RG 503H (lactide to glycolide ratio 50:50, molecular weight 24-38 kDa) was dissolved in 3.1 ml of THF and subsequently 200 µl of this solution were added to 20 ml of ultrapure water under sonication. The suspension was then concentrated at the rotary evaporator to a final volume of approximately 12 ml, resulting in a concentration of 0.167 mg/ml. The size distribution of prepared nanoparticles was measured using a Wyatt DynaPro DLS plate reader (Wyatt, Santa Barbara, USA), employing an 830 nm laser in a flat-bottom 384-well plate (Greiner, Frickenhausen, Germany) at 25 °C and 10 measurements were averaged per experiment.

MUH cytotoxicity assay – SH-SY5Y cells were seeded in 96-well plates (1 X 10^4 cells per well) and allowed to adhere overnight. The cells were subsequently treated with increasing doses of the indicated compounds for 24-48 h. Following exposure, the cells were washed with PBS and stained with 300 µg/ml MUH (prepared in DMSO, dissolved in PBS) for 30 min at 37°C. Cytotoxicity was read using a FlexStation 3.0 multi-well plate reader (Molecular Devices; excitation 360 nm, emission 460 nm, and cut-off 455 nm). Data were expressed relative to control.

PI exclusion assay – Cells were seeded in 12-well plates (1.0 X 10^5 cells per well) and the next day, the cells were treated with increasing doses of SPM, alone or in combination with the CTSB inhibitor CA-074 (25 µM, 1 h pre-incubation) or acidic nanoparticles (180 ng/ml, 1 h pre-incubation), and incubated for 24 h at 37°C. Thereafter, the cells were harvested following trypsinization and a brief centrifugation (300 x g; 5 min), washed with PBS and stained with 1 µg/ml PI (in PBS containing 1% BSA). An Attune Nxt (Thermo Fischer Scientific) flow cytometer was used to determine the proportion of PI-positive cells (10,000 events per treatment).

FITC-dextran based lysosomal pH – Adapted protocol from[51,52]. SH-SY5Y cells were seeded in 12-well plates (1.0 X 10^5 cells per well) and allowed to adhere overnight. Cells were exposed to 50 µg/ml FITC-dextran for 72 h. Samples were then washed, placed in fresh media for 2 h prior to treatment with SPM (10 µM) alone or in combination with acidic nanoparticles (180 ng/ml, 1 h pre-incubation) for a further 4 h. Samples were then collected by centrifugation (300 x g, 5 min) and washed in PBS. Cells were finally re-suspended in 500 µl of PBS containing 1% BSA and FITC dual emission was assessed by flow cytometry (excitation 488 nm, emission 530 nm (BL1) and 600 nm (BL2)) of 10,000 events per condition using an Attune NXT flow cytometer (Thermo Fisher Scientific). The emission ratio (BL1/BL2) of all samples were compared to a standard curve, whereby signals were obtained from untreated cells resuspended in monensin (100 µM) containing Britton Robinson buffer with increasing pH (3.0-8.0).

Lysosomal degradative capacity – Cell lines were seeded in 12-well plates (1.0 X 10^5 cells per well) and the next day, the cells were pre-treated with SPM (10 µM) for 1 h at 37°C. For samples requiring acidic nanoparticle exposure, cells were treated with 180 ng/ml 1 h prior to SPM addition. Subsequently, 5 µg/ml DQ-Green BSA was added to the cells for a further 3 h (37°C). Finally, the cells were collected (300 x g, 5 min), and the MFI of 10,000 events were assessed using an Attune Nxt (Thermo Fischer Scientific) flow cytometer.

Cathepsin activity assays – SH-SY5Y cells were seeded in 10 cm plates (2 X 10^6 cells per plate) and allowed to adhere overnight prior to treatment with 10 µM SPM for 4 h at 37°C. For samples requiring acidic nanoparticle addition, 180 ng/ml nanoparticles were added 1 h prior to SPM addition. Next, the samples were harvested using TRYPLE and a brief centrifugation (300 x g; 5 min). CTSB (ab65300) and CTSD (ab65302) activities were assessed using commercially available kits (Abcam) according to the manufacturer's instructions. MFI were acquired using a FlexStation 3.0 multi-well plate reader (Molecular Devices).

Lysosomal membrane integrity – SH-SY5Y cells were seeded in 12-well plates (1.0 X 10^5 cells per well) and the next day, the cells were incubated with 5 µg/ml AO (dissolved in media) for 15 min at

37°C. Thereafter, the medium was discarded, the cells were washed, and fresh medium was added. For samples requiring acidic nanoparticles, cells were treated with 180 ng/ml 1 h prior to SPM addition. The cells were then treated with 10 µM SPM for 4 h at 37°C. Finally, the cells were collected and resuspended in PBS containing 1% BSA. The MFI of 10,000 events was captured using an Attune Nxt (Thermo Fischer Scientific) flow cytometer.

BODIPY-SPM localization and lysosomal rupture analysis – For all immunofluorescent stainings SH-SY5Y cell lines were seeded in 12-well plates (0.25 X 10^5 cells per well on coverslips) and the next day, the cells were incubated with the indicated compounds for 4 h at 37°C. For BODIPY-SPM analysis, cells were pulsed with 5 µM SPM for 15 min, washed and chased in fresh media for a further 105 min at 37°C. Following treatments, the cells were washed twice in PBS, fixed in 4% paraformaldehyde for 30 min (37°C), washed in PBS and stored at 4°C. For immunofluorescence staining, the cells were washed in PBS containing 0.5% Tween 20 (PBS-T), permeabilized in PBS containing 0.1% Triton X-100 (30 min) and blocked first in 0.1 M glycine (1 h) and then in PBS-T containing 1% fetal calf serum and 10% BSA (30 min). Gal-3-, LAMP1- and cathepsin B-specific antibodies were used at a dilution of 1:100-200 (in PBS-T containing 1% BSA) overnight at 4°C. Subsequently, the samples were washed and incubated with Alexa Fluor™ secondary antibody (1:1,000; 30 min). To assess FITC-dextran release, cells were loaded with 50 µg/ml FITC-dextran for 72 h, cells were then washed and placed in fresh media for 1 h prior to SPM (10 µM) addition. To visualize the nucleus, all samples were stained with DAPI (200 ng/ml, 15 min). Following staining, the samples were fixed to slides, and images were acquired using an LSM780 or LSM880 confocal microscope (Zeiss). For the acquisition of BODIPY-SPM, images were taken with equal settings to confirm uptake potential of ATP13A2 (Extended data Fig. 1i). To assess the intracellular distribution of BODIPY-SPM (Fig. 2d and Extended data Fig. 1j-l), microscope settings were optimized per cell type to allow a comparable assessment of BODIPY-SPM localization in KO/WT and KO/D508N cells.

Neuron isolation – Primary cortical neurons were derived from E16 FVB/N mice embryos. Pregnant mice were sacrificed on gestation day 16 by cervical dislocation. E16 mice pup brains were collected and placed in a dish containing calcium- and magnesium-free Hanks' Balanced Salt Solution (HBSS,

Life Technologies, 14180-046) on ice. Both cerebral hemispheres were separated from the cerebellum. Meninges were removed from the cerebral hemispheres and the brain cortices dissected. Brain cortices were collected, washed twice and digested with 0.05% trypsin (Life Technologies, 25300-054, 10 min at 37°C). Trypsin reaction was terminated by the addition of 7 ml HBSS and 1 ml of horse serum. Cells were separated by pipetting and filtration through a cell strainer (40 µm, Falcon, 352340). Cells were centrifuged at 1,000 rpm for 5 min (4°C), the supernatant discarded and the pellet suspended in 5 ml Dulbecco's Modified Eagle Medium (DMEM; Sigma-Aldrich, D6546) containing GlutaMAX (Life Technologies, 31966-021) containing 5% horse serum (Life Technologies, 26050-088) and 20 mM glucose (Sigma-Aldrich, 8270). Primary cortical neurons were plated in 12 well plates, on cover slips coated with poly-D-lysine (Sigma-Aldrich, P6407). After an overnight incubation, cell medium was exchanged for Neurobasal medium (Life Technologies, 21103-049) supplemented with 2 mM L-glutamine (Life Technologies, 25030-24) and 2% B27 (Life Technologies, 17504-044).

Atp13a2 knockdown and rescue in isolated cortical neurons – For knockdown, microRNA (miR) based short-hairpin lentiviral vectors were generated as described[53]. The two most potent miR's against mouse Atp13a2 (mouse miR-3: CCACGCCGAAACACTCGTTATA and mouse miR-5: CGCCGAAACACTCGTTATAGAA) were used to induce knockdown in mouse primary neurons. A miR targeting firefly luciferase (Fluc) was used as a control (miR-Fluc, ACGCTGAGTACTTCGAAATGTC). Primary neurons were transduced 4 days after isolation, 72 h prior to experimentation. For rescue of ATP13A2 expression in knockdown conditions, neurons were subjected to a second round of transductions with either human WT or D508N variants of ATP13A2, 24 h post miR addition. Fluc was used as an overexpression control. At day 7 post-isolation, cells were treated with 10 µM SPM for 24h. To test the contribution of CTSB in SPM-induced cell death, neurons were pre-treated (30 min) with 10 µM CA-074. Knockdown efficiency was validated with qRT-PCR on mRNA levels 72h after transduction using the following primers (Atp13a2 Fw: CATGGCCCTCTACAGCCTGA; Atp13a2 Rv: CTCATGAGCACCGCAACCGT) with Gapdh as internal control (Fw: TGTGTCCGTCGTGGATCTGA; Rv: CCTGCTTCACCACCTTCTTGA). All mouse primary neuron experiments were carried out in accordance with the European Communities

Council Directive of November 24, 1986 (86/609/EEC) and approved by the Bioethical Committee of the KU Leuven (Belgium) (ECD project P185-2014).

TUNEL staining – TUNEL staining was assessed according to the manufacturer's protocol for the Click-iT Plus TUNEL assay (ThermoFisher, C10617). DAPI was used as a nuclear counterstain and images were acquired using a Leica LSM780 confocal microscope.

C. elegans **–** During routine culture, nematodes were grown on NGM (nematode growth medium) using *E. coli* strain AMA1004 as food source[54,55]. In order to reduce the likelihood that bacterial catabolism and divalent cations would interfere with SPD assays, these were done using DCDA (divalent cation depleted agar) plates, which do not permit bacterial growth. This medium contains; **a)** 2% agar (Carl Roth 5210) that has been washed with 50 mM EDTA, followed by multiple washes with reverse osmosis purified water, **b)** 50 mM HEPES pH 7.4 and **c)** 20 µg/ml kanamycin. Spermidine trihydrochloride (1 M stock solution; Sigma S2501) was added to a final concentration of 5 mM after microwaving to melt the agar. Assays were done in 35 mm plates that contained 1 ml of DCDA. Approximately 2 µl of *E. coli* was transferred to each assay plate from the lawn of a seeded NGM plate. In each case, multiple adult hermaphrodites were added to the assay plate and allowed to lay eggs for 8 h (data sets 1 and 3) or 15 h (data set 2) at 23.5°C, then removed. Incubation of plates at 23.5°C was continued until the 0 mM SPD N2 plates contained many mid-late stage L4s, at which point worms were rinsed off the plates and stored in microfuge tubes at -20°C. Worm lengths were determined by mounting the thawed (dead) animals on an agarose pad covered by a coverslip, capturing images using a Leica M205 FA microscope equipped with digital camera plus software, and measuring the length of each worm from snout to tail tip using Image J.

C. elegans expresses three ATP13A2 orthologues: CATP-5-7. Therefore in this study the following mutant alleles were used, each of which was backcrossed to N2 Bristol at least three times: *catp-6(ok3473)* IV, *catp-7(tm4438)* IV, *catp-5(tm4481)* X[56]. Each of these is a null allele, so they are referred to in the text as catp-#(0).

Transgenic strains carrying extrachromosomal arrays with the pRF4 *rol-6(su1006)* plasmid were generated by microinjection and maintained as described previously[57]. Injection mixes typically

contained 100 µg/ml pRF4, plus 30 µg/ml of the test construct. In some cases, *Pmyo-2::gfp* was included at approximately 5 µg/ml as an additional method for detecting transgenic animals. To generate transport-defective versions of *catp-6* and *catp-7*, plasmids carrying *catp-6::mKate2* and *catp-7::GFP*[22] were modified to change the coding sequence for the conserved DKTGT autophosphorylation motif to NKTGT. Proper expression and subcellular localization of CATP-6::mKate2 and CATP-7::GFP was verified in the case of all transgenic strains that were used (*catp-6(0);[catp-6(+)])* and *catp-7(0)*;*[catp-7(+)]* express CATP-6 and CATP-7 WT in the null background, respectively; *catp-6(0)*;*[catp-6(D465N)]* and *catp-7(0)*;*[catp-7(D503N)]* express CATP-6 D465N and CATP-7 D503N in the null background).

Statistics and Reproducibility– Data are expressed as the mean ± S.E.M. or with individual data points (replicates of multiple independent experiments) shown on group means or box whisker plots (indication of median, 25 percentile, 75 percentile and minimum to maximum value range). Flow cytometry was set up and gated as described in Supplementary Figure 2. GraphPad Prism 7.04 was used to plot all graphs and to perform all of the required statistical and quantitative assessments. Statistical tests for each graph are described in the legend. The number of independent biological experiments for each panel is highlighted in the figure legends. For the cell biological experiments using the SH-SY5Y CON, ATP13A2 KO, KO/WT and KO/D508N cell lines, each cell model is the sum of two independent clones, each performed a minimum of three independent times. For the quantification of immunoblots and radiograms, image J and Image Quant programmes were used. Experiments on various model systems were executed by different researchers, which provided consistent results that independently confirmed the major conclusions.

Reporting Summary – Further information on research design is available in the Nature research reporting summary linked to this paper.

Data availability

Gel source data for immunoblots and radiograms (Fig. 1-2, Extended Data Fig. 1-3, 6) are available with the online version of the paper (Supplementary Figure 1). All other datasets generated within this study

are presented and analysed within this manuscript and are available from the corresponding author upon reasonable request.

Methods References

31 Axelsen, K. B. & Palmgren, M. G. Evolution of substrate specificities in the P-type ATPase superfamily. *Journal of molecular evolution* **46**, 84-101 (1998).

32 Grunewald, A. *et al.* ATP13A2 mutations impair mitochondrial function in fibroblasts from patients with Kufor-Rakeb syndrome. *Neurobiol Aging* **33**, 1843 e1841-1847, doi:10.1016/j.neurobiolaging.2011.12.035S0197-4580(11)00580-X [pii] (2012).

33 Usenovic, M., Tresse, E., Mazzulli, J. R., Taylor, J. P. & Krainc, D. Deficiency of ATP13A2 leads to lysosomal dysfunction, alpha-synuclein accumulation, and neurotoxicity. *J Neurosci* **32**, 4240-4246, doi:32/12/4240 [pii]10.1523/JNEUROSCI.5575-11.2012 (2012).

34 Santoro, L. *et al.* Novel ATP13A2 (PARK9) homozygous mutation in a family with marked phenotype variability. *Neurogenetics* **12**, 33-39, doi:10.1007/s10048-010-0259-0 (2011).

35 Funayama, M. *et al.* Rapid screening of ATP13A2 variant with high-resolution melting analysis. *Mov Disord* **25**, 2434-2437, doi:10.1002/mds.23106 (2010).

36 Lin, C. H. *et al.* Novel ATP13A2 variant associated with Parkinson disease in Taiwan and Singapore. *Neurology* **71**, 1727-1732, doi:10.1212/01.wnl.0000335167.72412.6871/21/1727 [pii] (2008).

37 Mao, X. Y. *et al.* ATP13A2 G2236A variant is rare in patients with early-onset Parkinson's disease and familial Parkinson's disease from Mainland China. *Parkinsonism Relat Disord* **16**, 235-236, doi:10.1016/j.parkreldis.2009.11.010 (2010).

38 Sanjana, N. E., Shalem, O. & Zhang, F. Improved vectors and genome-wide libraries for CRISPR screening. *Nat Methods* **11**, 783-784, doi:10.1038/nmeth.3047 (2014).

39 Kleinstiver, B. P. *et al.* High-fidelity CRISPR-Cas9 nucleases with no detectable genome-wide off-target effects. *Nature* **529**, 490-495, doi:10.1038/nature16526 (2016).

40 Doench, J. G. *et al.* Optimized sgRNA design to maximize activity and minimize off-target effects of CRISPR-Cas9. *Nat Biotechnol* **34**, 184-191, doi:10.1038/nbt.3437 (2016).

41 Covy, J. P., Waxman, E. A. & Giasson, B. I. Characterization of cellular protective effects of ATP13A2/PARK9 expression and alterations resulting from pathogenic mutants. *J Neurosci Res* **90**, 2306-2316, doi:10.1002/jnr.23112 (2012).

42 Gitler, A. D. *et al.* Alpha-synuclein is part of a diverse and highly conserved interaction network that includes PARK9 and manganese toxicity. *Nature genetics* **41**, 308-315 (2009).

43 Kong, S. M. *et al.* Parkinson's disease-linked human PARK9/ATP13A2 maintains zinc homeostasis and promotes alpha-Synuclein externalization via exosomes. *Hum Mol Genet* **23**, 2816-2833, doi:10.1093/hmg/ddu099 (2014).

44 Lambie, E. J., Tieu, P. J., Lebedeva, N., Church, D. L. & Conradt, B. CATP-6, a C. elegans ortholog of ATP13A2 PARK9, positively regulates GEM-1, an SLC16A transporter. *PLoS One* **8**, e77202, doi:10.1371/journal.pone.0077202 (2013).

45 Tsunemi, T. *et al.* Increased Lysosomal Exocytosis Induced by Lysosomal Ca(2+) Channel Agonists Protects Human Dopaminergic Neurons from alpha-Synuclein Toxicity. *J Neurosci* **39**, 5760-5772, doi:10.1523/JNEUROSCI.3085-18.2019 (2019).

46 Gietz, R. D. & Woods, R. A. Transformation of yeast by lithium acetate/single-stranded carrier DNA/polyethylene glycol method. *Methods Enzymol* **350**, 87-96 (2002).

47 Azouaoui, H. *et al.* A high-yield co-expression system for the purification of an intact Drs2p-Cdc50p lipid flippase complex, critically dependent on and stabilized by phosphatidylinositol-4-phosphate. *PLoS One* **9**, e112176, doi:10.1371/journal.pone.0112176 (2014).

48 Jidenko, M., Lenoir, G., Fuentes, J. M., le Maire, M. & Jaxel, C. Expression in yeast and purification of a membrane protein, SERCA1a, using a biotinylated acceptor domain. *Protein Expr Purif* **48**, 32-42, doi:10.1016/j.pep.2006.03.001 (2006).
49 Papadopulos, A. *et al.* Flippase activity detected with unlabeled lipids by shape changes of giant unilamellar vesicles. *J Biol Chem* **282**, 15559-15568, doi:10.1074/jbc.M604740200 (2007).
50 Byun, J. A. *et al.* Analysis of polyamines as carbamoyl derivatives in urine and serum by liquid chromatography-tandem mass spectrometry. *Biomed Chromatogr* **22**, 73-80, doi:10.1002/bmc.898 (2008).
51 Stroikin, Y., Mild, H., Johansson, U., Roberg, K. & Ollinger, K. Lysosome-targeted stress reveals increased stability of lipofuscin-containing lysosomes. *Age* **30**, 31-42, doi:10.1007/s11357-007-9045-9 (2008).
52 Nilsson, C., Kagedal, K., Johansson, U. & Ollinger, K. Analysis of cytosolic and lysosomal pH in apoptotic cells by flow cytometry. *Methods in cell science : an official journal of the Society for In Vitro Biology* **25**, 185-194, doi:10.1007/s11022-004-8228-3 (2003).
53 Osorio, L. *et al.* Viral vectors expressing a single microRNA-based short-hairpin RNA result in potent gene silencing in vitro and in vivo. *Journal of biotechnology* **169**, 71-81, doi:10.1016/j.jbiotec.2013.11.004 (2014).
54 Brenner, S. The genetics of Caenorhabditis elegans. *Genetics* **77**, 71-94 (1974).
55 Casadaban, M. J., Martinez-Arias, A., Shapira, S. K. & Chou, J. Beta-galactosidase gene fusions for analyzing gene expression in escherichia coli and yeast. *Methods Enzymol* **100**, 293-308 (1983).
56 Consortium, C. e. D. M. large-scale screening for targeted knockouts in the Caenorhabditis elegans genome. *G3 (Bethesda)* **2**, 1415-1425, doi:10.1534/g3.112.003830 (2012).
57 Mello, C. C., Kramer, J. M., Stinchcomb, D. & Ambros, V. Efficient gene transfer in C.elegans: extrachromosomal maintenance and integration of transforming sequences. *EMBO J* **10**, 3959-3970 (1991).
58 Roy, A., Kucukural, A. & Zhang, Y. I-TASSER: a unified platform for automated protein structure and function prediction. *Nat Protoc* **5**, 725-738, doi:10.1038/nprot.2010.5 (2010).
59 Zhang, Y. I-TASSER server for protein 3D structure prediction. *BMC Bioinformatics* **9**, 40, doi:10.1186/1471-2105-9-40 (2008).
60 Omasits, U., Ahrens, C. H., Muller, S. & Wollscheid, B. Protter: interactive protein feature visualization and integration with experimental proteomic data. *Bioinformatics* **30**, 884-886, doi:10.1093/bioinformatics/btt607 (2014).

Acknowledgements

This work was funded by the Fonds Wetenschappelijk Onderzoek (FWO, Research Foundation Flanders) (G094219N to P.V., G092714 and G080517N to V.Ba., SBO Neuro-TRAFFIC S006617N to V.Ba., P.V., W.A., and J.V.S.; and 1503117N to S.M.), the KU Leuven (OT/13/091; LysoCaN C16/15/073 to P.V., J.V.S., W.A. and P.A.; OT/14/120 to V.Ba.), and the Queen Elisabeth Medical Foundation for Neurosciences (P.V. and V.Ba.). S.v.V. is an aspirant FWO research fellow (11Y7518N) and J.P.K. recipient of a doctoral grant strategic basic research of the FWO (1S18518N). J.L. received Lundbeck postdoctoral fellowships R209-2015-2704 and R171-2014-663. Funding for E.J.L. and J.Z.

was provided by DFG grant LA3380/2-1. Some nematode strains were provided by the CGC, which is funded by NIH Office of Research Infrastructure Programs (P40 OD010440). We thank Dr. P.P. Van Veldhoven (KU Leuven) for discussions and Dr. P. Chaltin (Center for Drug Design and Discovery) for financial support for V.Be. We thank M. Schuermans, T. Arslan, A. Florizoone, J. Van Asselberghs, J. Chen and N. Hamouda for their technical assistance. We also acknowledge our frequent use of the facilities and equipment of the Leuven Viral Vector Core facility (KU Leuven), Mass Spectrometry Core (Dr. R. Derua, KU Leuven), Cell and Tissue Imaging Cluster (Dr. P. Vanden Berghe, KU Leuven) and the FACS Core (KU Leuven/VIB).

Author contributions

The study was conceived and designed by P.V., S.M., S.v.V. and J.E.; C.V.d.H. generated all stable cell lines and analysed ATP13A2 knockdown; J.P.D. performed and analysed the CRISPR experiments; R.V. and J.P.K. synthesized BODIPY-labelled polyamine analogues; J.P.K performed and analysed acidic nanoparticle preparations; S.v.V performed and analysed the biochemical experiments (except Extended Data Fig. 2f by V.Be.); J.L. contributed to ATP13A2 purification protocol; S.M. performed and analysed the cell biology experiments; B.G. performed metabolomics; G.G. isolated mouse neurons; E.L. and J.Z. performed *C. elegans* experiments; P.V., S.v.V. and S.M. wrote the manuscript, which was reviewed by all authors.

Patent WO-2018002350-A1 of KU Leuven describes methods for detecting compounds with therapeutic use that target ATP13A2 or related isoforms using biological material and assays described in the current manuscript.

Competing interests

The authors declare no competing interests.

Additional information

Supplementary information is available for this paper at XXXX.

Correspondence and requests for materials should be addressed to P.V.

Peer review information

Reprints and permissions information is available at www.nature.com/reprints.

Extended Data Figure/Table legends

Extended Data Table 1 – Apparent K_m and V_{max} values for ATP13A2 in the presence of various polyamines. Data are derived from Fig. 1b, f and Extended Data Figure 1e. Data are N = 3 (Spermidine, N1-acetylspermine), or N=6 (Spermine) biologically independent experiments. * Estimated values (could not be accurately determined following fitting of the curve).

Extended Data Figure 1 – ATP13A2 is a polyamine transporter.

ATP13A2 ATPase activity was measured in solubilized microsomes (5 µg) harvested from SH-SY5Y cells stably overexpressing ATP13A2 WT (WT-OE) in the presence of **(a)** 100 nM $CaCl_2$, $MnCl_2$, $ZnCl_2$ or $FeCl_3$ and 100 µM SPD or SPM (D508N-OE as a negative control, WT was referenced from Fig. 1b) or in the presence of the indicated doses of **(b)** inorganic ions and heavy metals $CaCl_2$, $MnCl_2$, $ZnCl_2$ or $FeCl_3$; **(c)** diamines (cadaverine, agmatine and amino-acid L-arginine); **(d)** monoamines (dopamine and histamine); and **(e)** acetylated polyamines (N^1-acetylspermine, N^8-acetylspermidine, or N^1-acetylspermidine). As a reference for **(c-e)**, we plotted the dose-response curve of SPM from Fig. 1b. **(f)** 20 µg of microsomes harvested from SH-SY5Y cells that overexpress ATP13A2 were incubated for 60 s with [γ-^{32}P] ATP in the presence of 10 mM ornithine (ORN) or SPM (referenced from Fig. 1c). The left panel shows a representative autoradiogram of the phospho-enzymes (EP), while the right panel depicts the quantification. **(g)** ATPase activity of purified ATP13A2 was assessed following 1 mM SPM +/- 0.25 mM orthovanadate (ORTH), a general P-type ATPase inhibitor (supplemented with 125 µM PA/PI(3,5)P2; conditions (-) and (-)/SPM refer to Fig. 1f). **(h)** Purified ATP13A2 was incubated with [γ-^{32}P] ATP in the presence of 1 mM SPM, and radioactivity (phospho-intermediate) assessed by scintillation counting. **(i)** Confocal microscopy comparison of pulse (5 µM, 15 min) chase (105 min, medium) BODIPY-SPM uptake in KO/WT and KO/D508N cell lines. Cells were subsequently stained with LAMP1 and imaged with the same laser settings by confocal microscopy. DAPI was used to

visualize the nucleus. Scale bar = 5 µm. **(j)** Line intensity plots of indicated dashed lines in (Fig. 2d). **(k)** Pearson's coefficient analysis of LAMP1/BODIPY-SPM of images in Fig. 2d (KO/WT; 78 images *vs.* KO/D508N; 85 images). **(l)** Mean fluorescent intensities of BODIPY in DAPI positive regions of samples in Fig. 2d (KO/WT; 233 nuclei *vs.* KO/D508N; 243 nuclei). MFI, mean fluorescence intensities. (-), vehicle treated sample. Data are presented as the mean ± S.E.M. or mean with individual data points shown (points represent replicates), where N (number of independent biological experiments) equals N = 3. Analysis by one-way ANOVA with Dunnett's (**f**) or Tukey's (**a**, **g**) corrections, or by two-tailed t-test (unpaired, **h** or Welch's, **k-l**). Fitted lines: semi-log line (**b**) or nonlinear allosteric sigmoidal (**c-e**). For gel source data, see Supplementary Figure 1.

Extended Data Figure 2 – Streptavidin-based purification of ATP13A2 WT and catalytically dead E343A mutant. (a) Coomassie staining showing the ATP13A2 WT purification process, starting from solubilized yeast membrane fractions, followed by streptavidin affinity chromatography and on-column thrombin cleavage to elute the protein. **(b)** Western blot analysis of ATP13A2 purification. **(c)** Bar graph depicts protein purity as determined by densitometry of Coomassie-stained SDS-PAGE. **(d)** Mass spectrometry analysis of the purified ATP13A2 sample. Single, double and triple charged species are indicated. **(e)** To evaluate phospho-enzyme formation, yeast P3 membranes (20 µg) and purified ATP13A2 (1 µg) were incubated for 60 s with [γ-^{32}P] ATP. As a positive control, microsomes harvested from SH-SY5Y cells that overexpress ATP13A2 WT (20 µg) were used. The provided image is a representative radiogram depicting the ATP13A2 phospho-enzyme (EP). **(f)** The ATPase activity of purified ATP13A2 (0.3 µg) was measured in the presence of 2 mM SPM and the indicated concentrations of the ATP13A2 regulatory lipids phosphatidic acid (PA) and phosphatidylinositol(3,5)bisphosphate (PI(3,5)P2). **(g)** Coomassie staining showing the ATP13A2 E343A purification process. **(h)** The ATPase activity of purified ATP13A2 WT or E343A (0.5 µg) was measured in the presence of the indicated concentrations of SPM with 125 µM phosphatidic acid and 125 µM phosphatidylinositol(3,5)bisphosphate. Data are expressed as mean with individual data points (points represent replicates) (**c, h**). The values of N (independent biological experiments) equals N = 3:

b, **e-h**; N = 6: **d**; and N = 22: **a**, **c**. Analysis by one-way ANOVA with Tukey's post hoc correction (**h**). For gel source data, see Supplementary Figure 1.

Extended Data Figure 3 – Confirmation of CRISPR/Cas9-mediated ATP13A2 KO and subsequent rescue with ATP13A2 WT or D508N. (a) The ATP13A2 KO cell lines (KO) were generated by CRISPR/Cas9 in SH-SY5Y cells and confirmed by qRT-PCR (top) and immunoblotting (bottom). ATP13A2 mRNA expression was normalized to HPRT and TBP, while GAPDH was used as a loading control for the ATP13A2 protein levels. Two fragments of the same blot are depicted and separated by a dotted line. **(b)** Rescue of ATP13A2 KO was performed by lentiviral transduction to express ATP13A2 WT (KO/WT) and the catalytically dead mutant D508N, which was used as a negative control (KO/D508N). The expression of the ATP13A2 constructs was confirmed via immunoblotting. The number of biologically independent experiments equals N = 1: **a** (upper panel); or N = 3: **a** (lower panel), **b**. For gel source data, see Supplementary Figure 1.

Extended Data Figure 4 – ATP13A2 polyamine uptake complements cytosolic polyamine synthesis. (a-c) Flow cytometry assessment of the cellular uptake of BODIPY-labelled polyamine analogues **(a**, **b)** or FITC-dextran **(c)**. Uptake of BODIPY-SPD **(a)** or BODIPY-SPM **(b)** in SH-SY5Y cells overexpressing firefly luciferase (Fluc, negative control), ATP13A2 WT (WT-OE) or the catalytically dead mutant D508N (D508N-OE). The cells were incubated with 5 µM BODIPY-SPM or -SPD for 2 h prior to flow cytometric analysis. **(c)** Analysis of FITC-dextran uptake (measure of endocytic capacity) was performed in SH-SY5Y control (CON) cells with endogenous ATP13A2 expression, ATP13A2 KO cells (KO) and rescue cell lines with expression of ATP13A2 WT (KO/WT) or the D508N mutant (KO/D508N). The cells were pre-treated (30 min) with a combination (combo) of endocytosis inhibitors Dynasore (100 µM), Genistein (50 µM) and Pitstop 2 (50 µM). The cells were incubated for an additional 2 h with FITC-dextran at 37°C, followed by FACS analysis. **(d)** Schematic representation of polyamine synthesis. ORN, ornithine; PUT, putrescine; SPD, spermidine; SPM, spermine; ODC, ornithine decarboxylase; SRM, spermidine synthase; SMS, spermine synthase. Specific inhibitors are indicated in red (ODC inhibitor DFMO, D,L-alpha-difluoromethylornithine; SRM inhibitor 4MCHA, cis-4-methylcyclohexylamine; and SMS inhibitor APCHA, N-(3-

aminopropyl)cyclohexylamine). CON, KO, KO/WT or KO/D508N cells were subjected to inhibition of polyamine synthesis by DFMO **(e)**, 4MCHA **(f)** and APCHA **(g)** prior to measuring cell viability via MUH (4-methylumbelliferyl heptanoate) assay. All data represent the average of two independent CRISPR/Cas9 KO and control clones. All data are presented as means with data points overlaid (points represent replicates) or ± S.E.M. The value of N (biologically independent experiments) was N = 3: (**a-b**); or N = 4: (**c**, **e-g**). According to one-way ANOVA with Dunnett's post hoc correction (**a**-**b**) or Tukey's multiple comparison (**c**) or two-way ANOVA with Dunnett's (**e-g**). Fitted lines: nonlinear log(inhibitor) *vs*. response (variable slope) (**e-g**).

Extended Data Figure 5 – ATP13A2 catalytic and clinical mutations perturb polyamine function. **(a)** Sequence alignment of predicted transmembrane helices M4, M6 and M8. The alignment was generated using Clustal Omega. We generated mutants in M4 (A467V), M6 (D962N), and M8 (K1062A). The A467V mutation converts PPALP of the predicted substrate binding site in transmembrane segment M4 into PPVLP that is present in ATP13A5[4,30]. Also neighbouring membrane helices contribute to substrate coordination in P-type ATPases, which often relies on conserved and charged residues, such as D962 in M6 and K1062 in M8 of ATP13A2[4]. **(b)** Densitometry of the expression of catalytic mutants presented in Fig. 2e. **(c)** Flow cytometric analysis of cellular BODIPY-SPD uptake in SH-SY5Y cells overexpressing ATP13A2 WT, D508N or catalytic mutants. **(d)** Quantification of ATP13A2 phosphorylation levels (EP) presented in Fig 2g. **(e)** Densitometry of the expression of disease related mutants presented in Fig. 2i. **(f)** Flow cytometric analysis of cellular BODIPY-SPD uptake in SH-SY5Y cells overexpressing ATP13A2 WT, D508N or disease mutants. **(g)** Quantification of ATP13A2 phosphorylation levels presented in Fig. 2k. All data are depicted as means with individual data points (points represent replicates). The values of N (independent biological experiments) were N = 3: **b-c**, **d** (D508N (SPM), A467V (SPM), D962N (SPM), and K1062A (SPM)), **e** (T12M, G872R), **f**, **g** (T12M (-), T12M (SPM), T512I (SPM), G528R (SPM), A741T (SPM), and G872R (SPM)); N = 4: **d** (D508N (-), A467V (-), D962N (-), and K1062A (-)), **e** (WT, T512I, G528R, A741T), **g** (WT (-), T512I (-), G528R (-), A741T (-), and G872R (-)); N = 5: **d** (WT (-)); N = 6: **d** (WT

(SPM)), **g** (WT (SPM)). Analysis by one-way ANOVA with Dunnett's (**b-c**, **e-f**) or two-way ANOVA with Sidak's (**d**, **g**) post hoc corrections.

Extended Data Figure 6 – ATP sensitivity of ATP13A2 mutants D962N and E343A is SPM-independent. (a) Overview of rate constants of ATP13A2 phospho-enzyme decay following a chase with non-radioactive ATP with or without 1 mM SPM. **(b)** Following 30 s of incubating D962N microsomes (20 µg) with [γ-^{32}P] ATP, the time course of dephosphorylation after an ATP chase was measured in the presence or absence of spermine (SPM). The upper panel shows a representative autoradiogram of the phospho-enzymes (EP), while the lower panel depicts the quantification of ATP13A2 phosphorylation levels. As a reference, we plotted the WT curve, shown in Fig. 1d. Data are presented as the mean ± S.E.M. N = 4 biologically independent experiments. Analysis by two-way ANOVA with Tukey's test (**b**). Fitted line: two phase decay (**b**). For gel source data, see Supplementary Figure 1.

Extended Data Figure 7 – Predicted ATP13A2 topology. (a) Homology model of ATP13A2 based on the structure of Na^+/K^+-ATPase (ATP1A1, PDB file 3A3Y) as a template, generated by iTASSER (https://zhanglab.ccmb.med.umich.edu/I-TASSER/)[58,59]. **(b)** Predicted membrane topology of ATP13A2 visualized by Protter[60] (http://wlab.ethz.ch/protter). ATP13A2 consists of 10 transmembrane helices (M1-10) and an N-terminal membrane-associated region (Ma)[9]. Kufor-Rakeb syndrome [KRS]-associated mutations are highlighted in red; early-onset Parkinson's disease [EOPD]-associated mutations in green; hereditary spastic paraplegia [HSP]-associated mutations in light blue; neuronal ceroid lipofuscinosis [NCL]-associated mutations in orange. Catalytic mutations and mutations in the predicted substrate-binding region were highlighted as dark blue. Residues that were subjected to mutagenesis in this study are labelled. P-type ATPase signature motifs in the cytosolic domains are indicated in pink (only in **b**).

Extended Data Figure 8 – Lysosomal functionality and recovery. The impact of exogenous polyamines on cell toxicity (24 h) and lysosomal functionality (4 h) was assessed in SH-SY5Y control cells (CON) with endogenous ATP13A2, ATP13A2 KO cells (KO) and rescue cell lines with WT expression (KO/WT) or expression of the catalytically dead mutant D508N (KO/D508N) on the KO

background. Cytotoxicity of spermidine (SPD) **(a)**, spermine (SPM) **(b),** ornithine (ORN) **(c)** and putrescine (PUT) **(d)** were assessed via a 4-methylumbelliferyl heptanoate (MUH) cell viability assay. **(e)** Cell death of the aforementioned cells was assessed after 4 h SPM exposure (10 μM) by propidium iodide (PI) based flow cytometry. **(f)** Measurement of cathepsin D activity. **(g-h)** Lysosomal rupture under basal (-) and SPM (10 μM) conditions was assessed via loss of FITC-dextran (FITC-DEX) punctae **(g)**, or loss of cathepsin B (CTSB)/Lamp1 co-localization **(h)**. Confocal images depict representative images with or without SPM exposure (4 h, DAPI staining for nuclei was included as a reference). Scale bar, 10 μm. The box and whisker plots in **(g)** depict the frequency (left) and size (right) of FITC-DEX punctae; in **(h)** the Pearson coefficient of co-localization of CTSB and Lamp1. **(i)** Lysosomal pH (Fig. 3b) was evaluated using the fluorescent probe FITC-dextran and a dual-emission ratio-metric technique. FITC is excited at 488 nm and emission analyzed at 530 nm (BL1) and 610 nm (BL2). A pH calibration curve was generated using FITC-dextran in cells permeabilized with 100 μM monensin and equilibrated with calibration buffers (pH 3-8). **(j)** Representative size distribution of the acidic nanoparticles used in this study. (-), vehicle treated. Data are presented as the mean ± S.E.M. (**a-d**, **i**) or individual data points (representing replicates) overlaid on group means **(e)** or box and whisker plots (**f-h,** line = median, 25/75 percentiles). The values of N (independent biological experiments) were N = 3: (**e-j**); and N = 4: (**a-d**). Analysis by two-way ANOVA with Dunnett's (**a-b**) or Bonferroni's (**c-d**), or one-way ANOVA with Dunnett's (**e**), Sidak's (**f-g** (right)**)** or Tukey's post hoc corrections (**g** (left), **h**). Fitted lines: nonlinear log(inhibitor) *vs.* response (variable slope) (**a-b**).

Extended Data Figure 9 – Inhibition of cathepsin B activity attenuates SPM-induced neuronal death. The effect of cathepsin B inhibitor (CA-074, 10 μM) on SPM-induced (10 μM, 24 h) cell death in control (miR-Fluc) and Atp13a2 knockdown (miR-3 and miR-5) neurons was assayed via TUNEL-based staining. Left, representative confocal images; right, box and whiskers plot depicting TUNEL positivity. Data are presented as box and whisker (line = median, 25/75 percentiles) plots for which individual data points (representing replicates) are shown (N = 3 biologically independent experiments). Analysis by one-way ANOVA with Tukey's post hoc correction.

Figure 1

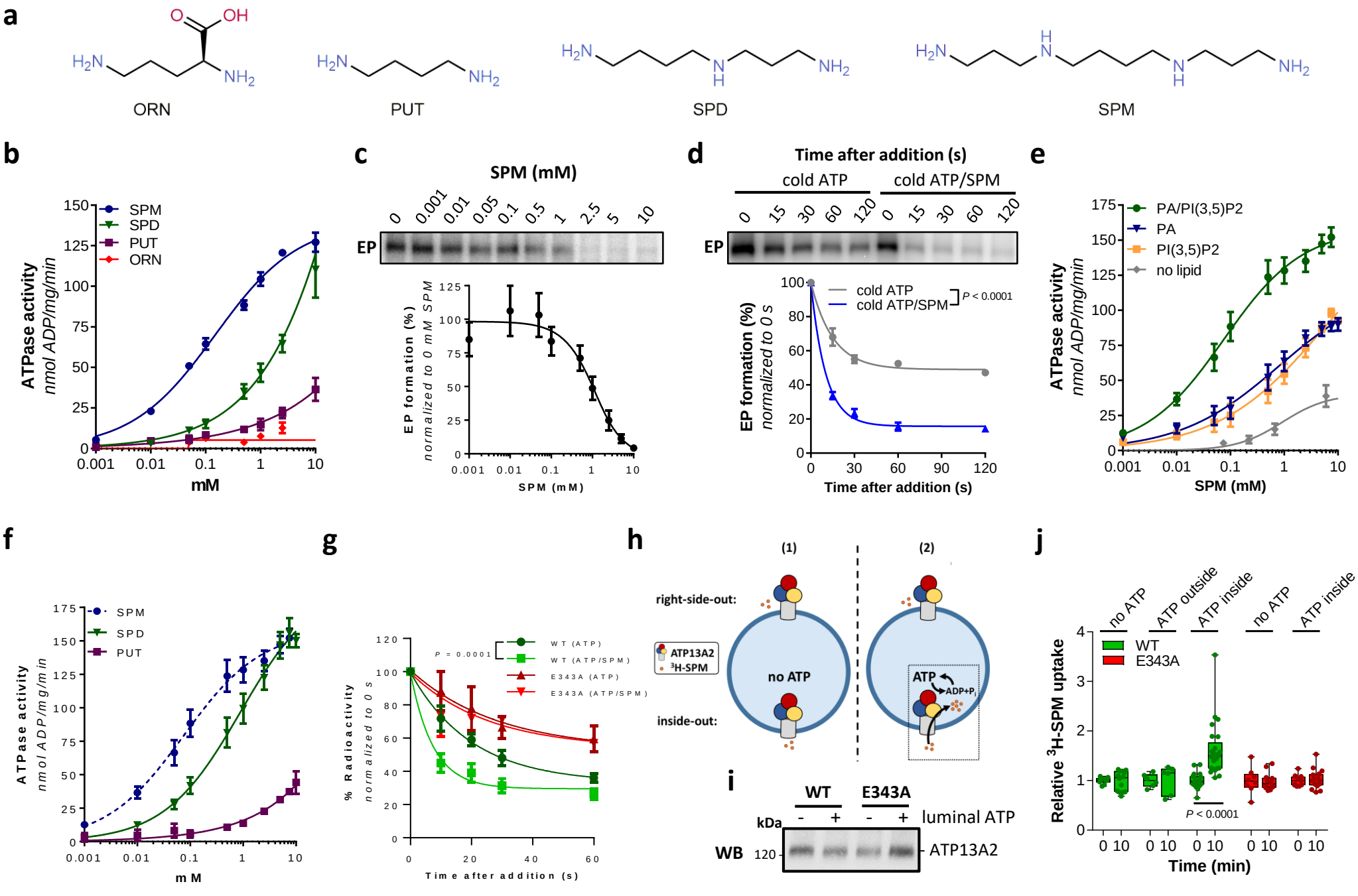
a
ORN
PUT
SPD
SPM
b
ATPase activity
nmol ADP/mg/min
SPM
SPD
PUT
ORN
mM
c
SPM (mM)
0 0.001 0.01 0.05 0.1 0.5 1 2.5 5 10
EP
EP formation (%)
normalized to 0 mM SPM
SPM (mM)
d
Time after addition (s)
cold ATP
cold ATP/SPM
0 15 30 60 120 0 15 30 60 120
EP
EP formation (%)
normalized to 0 s
cold ATP
cold ATP/SPM
P < 0.0001
Time after addition (s)
e
ATPase activity
nmol ADP/mg/min
PA/PI(3,5)P2
PA
PI(3,5)P2
no lipid
SPM (mM)
f
ATPase activity
nmol ADP/mg/min
SPM
SPD
PUT
mM
g
% Radioactivity
normalized to 0 s
P = 0.0001
WT (ATP)
WT (ATP/SPM)
E343A (ATP)
E343A (ATP/SPM)
Time after addition (s)
h
(1)
(2)
right-side-out:
ATP13A2
3H-SPM
no ATP
ATP
ADP+Pi
inside-out:
i
WT
E343A
kDa
- + - +
luminal ATP
WB
120
ATP13A2
j
no ATP
ATP outside
ATP inside
no ATP
ATP inside
WT
E343A
Relative 3H-SPM uptake
P < 0.0001
0 10 0 10 0 10 0 10 0 10
Time (min)

Figure 2

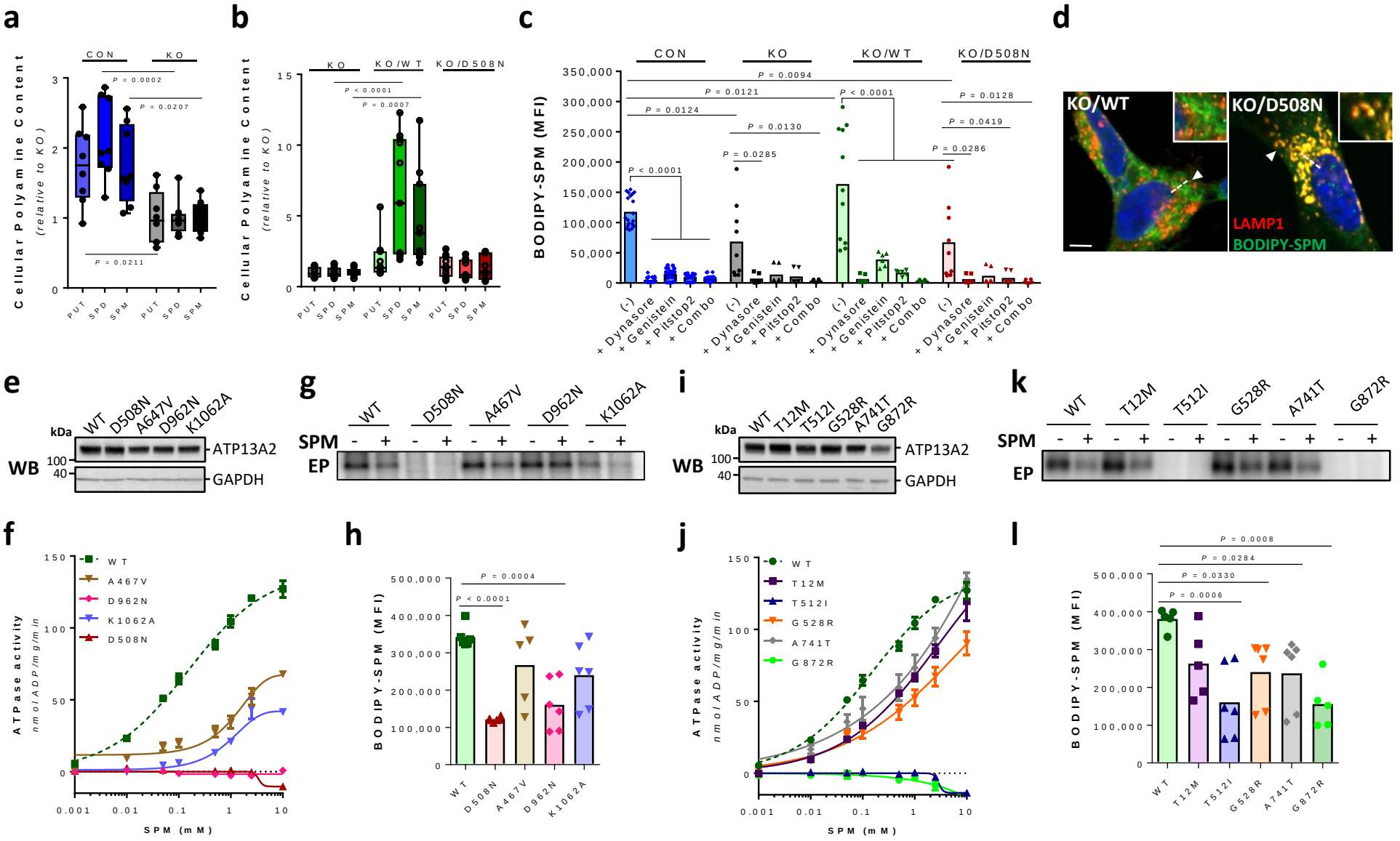
a
b
c
d
e
f
g
h
i
j
k
l
CON
KO
KO/WT
KO/D508N
Cellular Polyamine Content (relative to KO)
PUT
SPD
SPM
P = 0.0002
P = 0.0207
P = 0.0211
P < 0.0001
P = 0.0007
BODIPY-SPM (MFI)
P = 0.0094
P = 0.0121
P = 0.0124
P = 0.0130
P = 0.0285
P < 0.0001
P = 0.0128
P = 0.0419
P = 0.0286
(-)
+ Dynasore
+ Genistein
+ Pitstop2
+ Combo
KO/WT
KO/D508N
LAMP1
BODIPY-SPM
kDa
WB
ATP13A2
GAPDH
WT
D508N
A647V
D962N
K1062A
SPM
EP
T12M
T512I
G528R
A741T
G872R
ATPase activity nmol ADP/mg/min
SPM (mM)
P = 0.0004
P < 0.0001
P = 0.0008
P = 0.0284
P = 0.0330
P = 0.0006

Figure 3

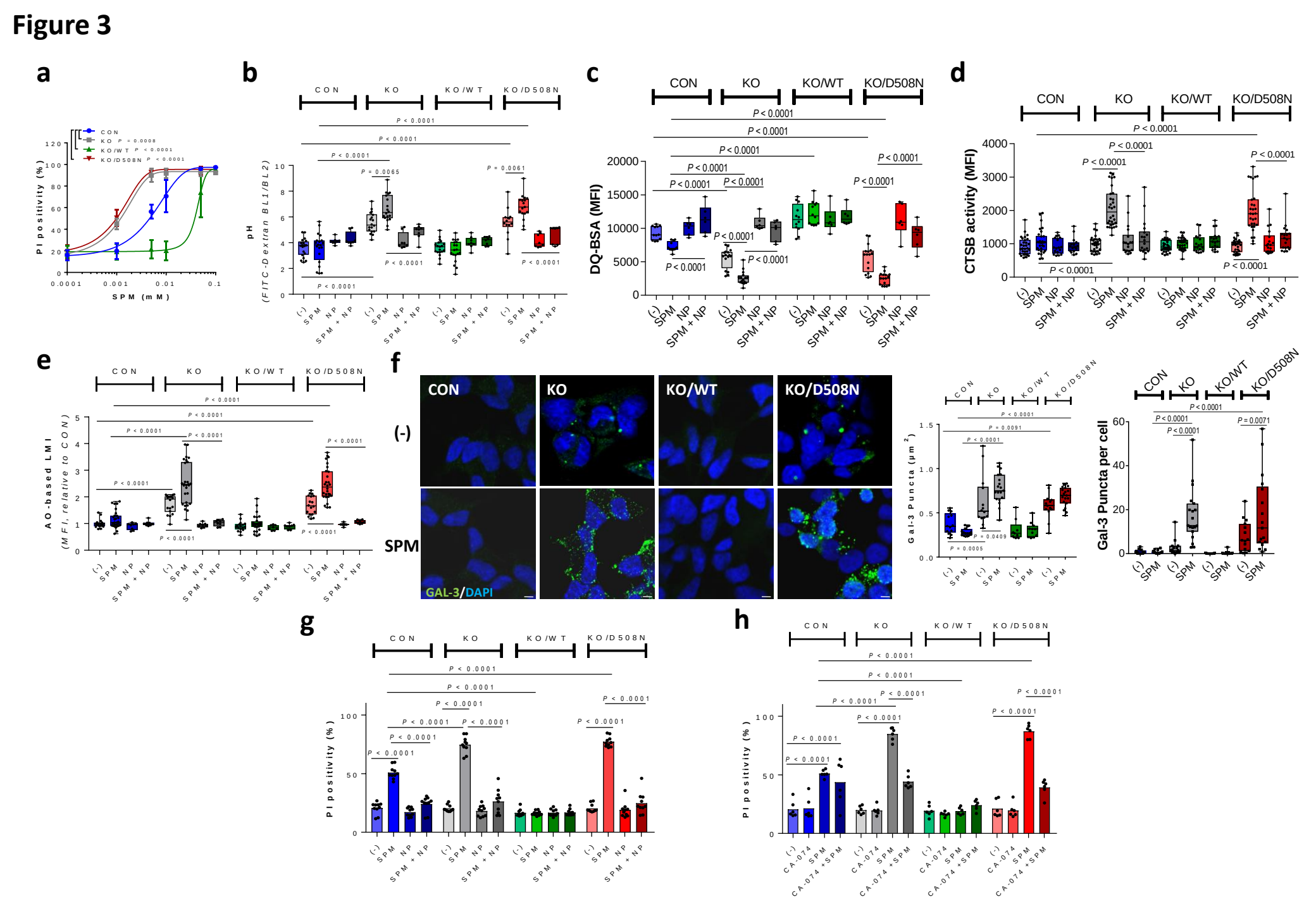
a
b
c
d
e
f
g
h
CON
KO
KO/WT
KO/D508N
SPM (mM)
PI positivity (%)
pH (FITC-Dextran BL1/BL2)
DQ-BSA (MFI)
CTSB activity (MFI)
AO-based LMI (MFI, relative to CON)
Gal-3 Puncta (μm²)
Gal-3 Puncta per cell
(-)
SPM
NP
SPM + NP
CA-074
CA-074 + SPM
GAL-3/DAPI

Figure 4

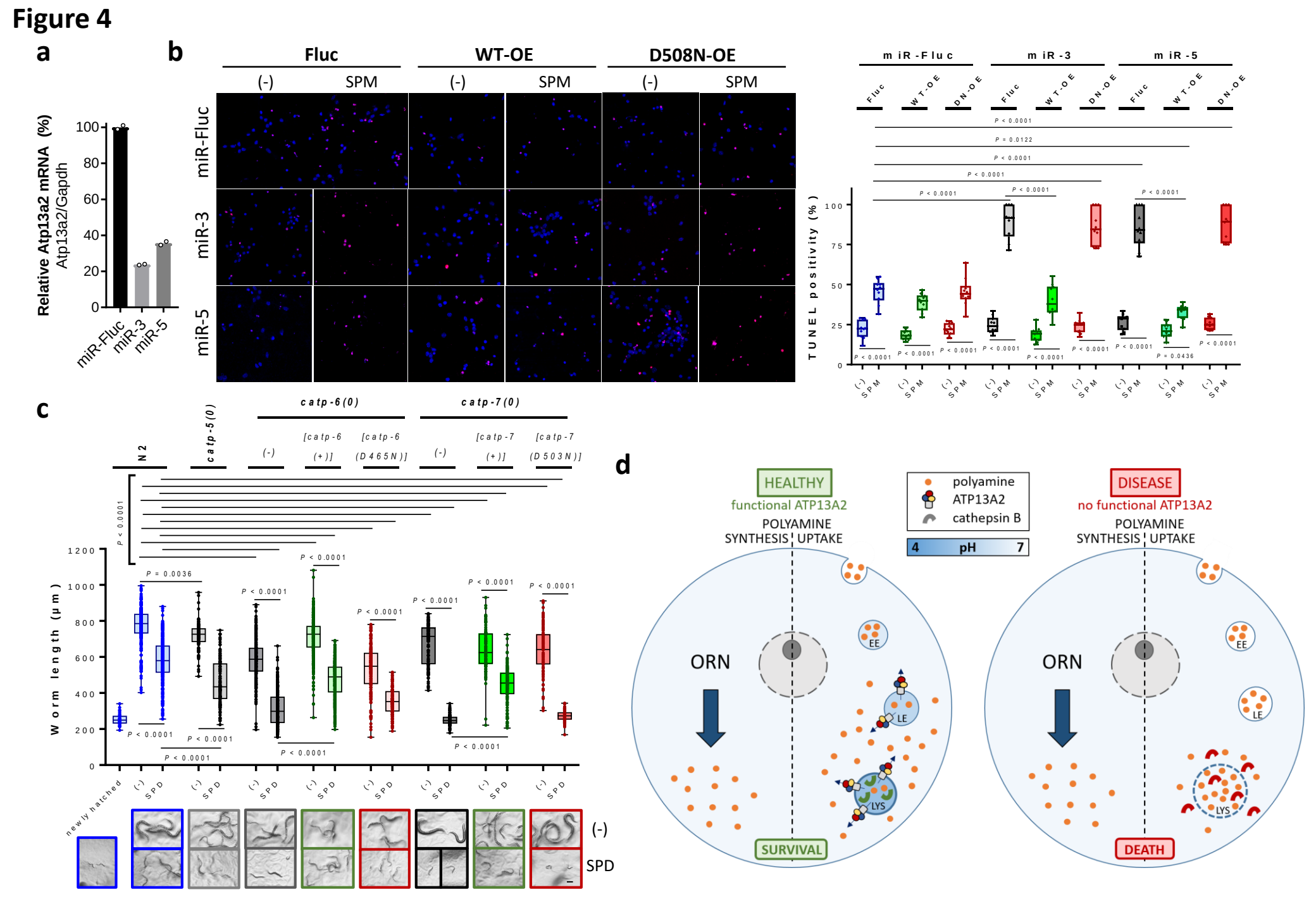
a
Relative Atp13a2 mRNA (%)
Atp13a2/Gapdh
100
80
60
40
20
0
miR-Fluc
miR-3
miR-5
b
Fluc
WT-OE
D508N-OE
(-)
SPM
miR-Fluc
miR-3
miR-5
miR-Fluc
miR-3
miR-5
Fluc
WT-OE
DN-OE
P < 0.0001
P = 0.0122
P < 0.0001
P < 0.0001
P < 0.0001
P < 0.0001
P < 0.0001
P < 0.0001
P = 0.0436
TUNEL positivity (%)
100
75
50
25
0
c
N2
catp-5(0)
catp-6(0)
catp-7(0)
(-)
[catp-6 (+)]
[catp-6 (D465N)]
(-)
[catp-7 (+)]
[catp-7 (D503N)]
P < 0.0001
Worm length (μm)
1200
1000
800
600
400
200
0
P = 0.0036
P < 0.0001
P < 0.0001
P < 0.0001
P < 0.0001
P < 0.0001
P < 0.0001
P < 0.0001
P < 0.0001
P < 0.0001
newly hatched
(-)
SPD
(-)
SPD
d
HEALTHY
functional ATP13A2
POLYAMINE
SYNTHESIS | UPTAKE
ORN
EE
LE
LYS
SURVIVAL
polyamine
ATP13A2
cathepsin B
4
pH
7
DISEASE
no functional ATP13A2
POLYAMINE
SYNTHESIS | UPTAKE
ORN
EE
LE
LYS
DEATH

Extended Data Table 1

Extended Data Table 1 – Overview of the apparent K_m and V_{max} values for ATP13A2 in the presence of relevant polyamines

	K_m ± SEM (µM)		V_{max} ± SEM (nmol ADP/mg/min)	
	Microsomal ATP13A2	**Purified ATP13A2**	**Microsomal ATP13A2**	**Purified ATP13A2**
Spermine	149 ± 34	76 ± 26	140 ± 6	159 ± 10
N^1-acetylspermine	286 ± 48	not tested	98 ± 5	not tested
Spermidine	~ 1700*	890 ± 501	~ 106*	194 ± 26

Extended Data Figure 1

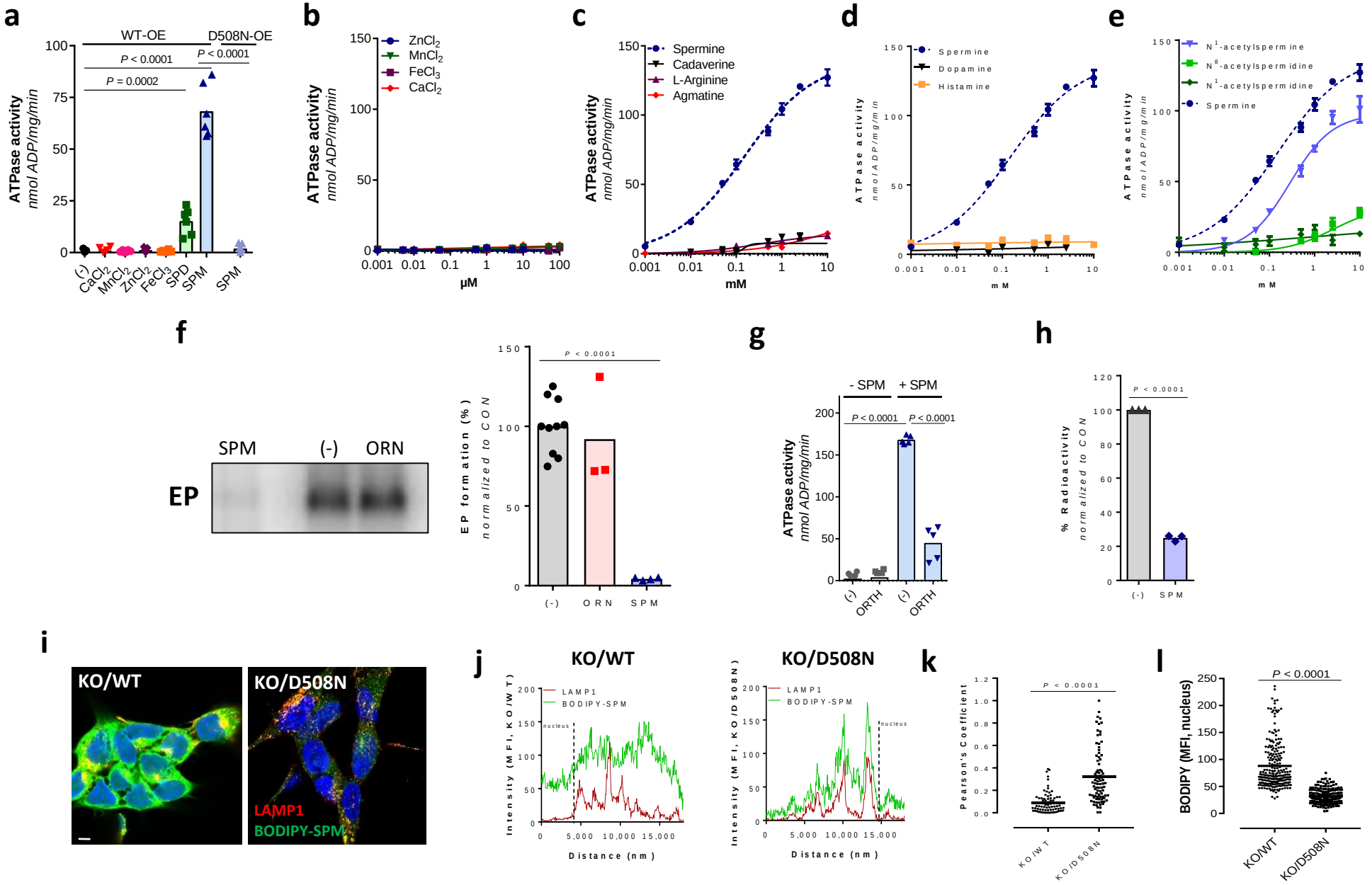

Extended Data Figure 2

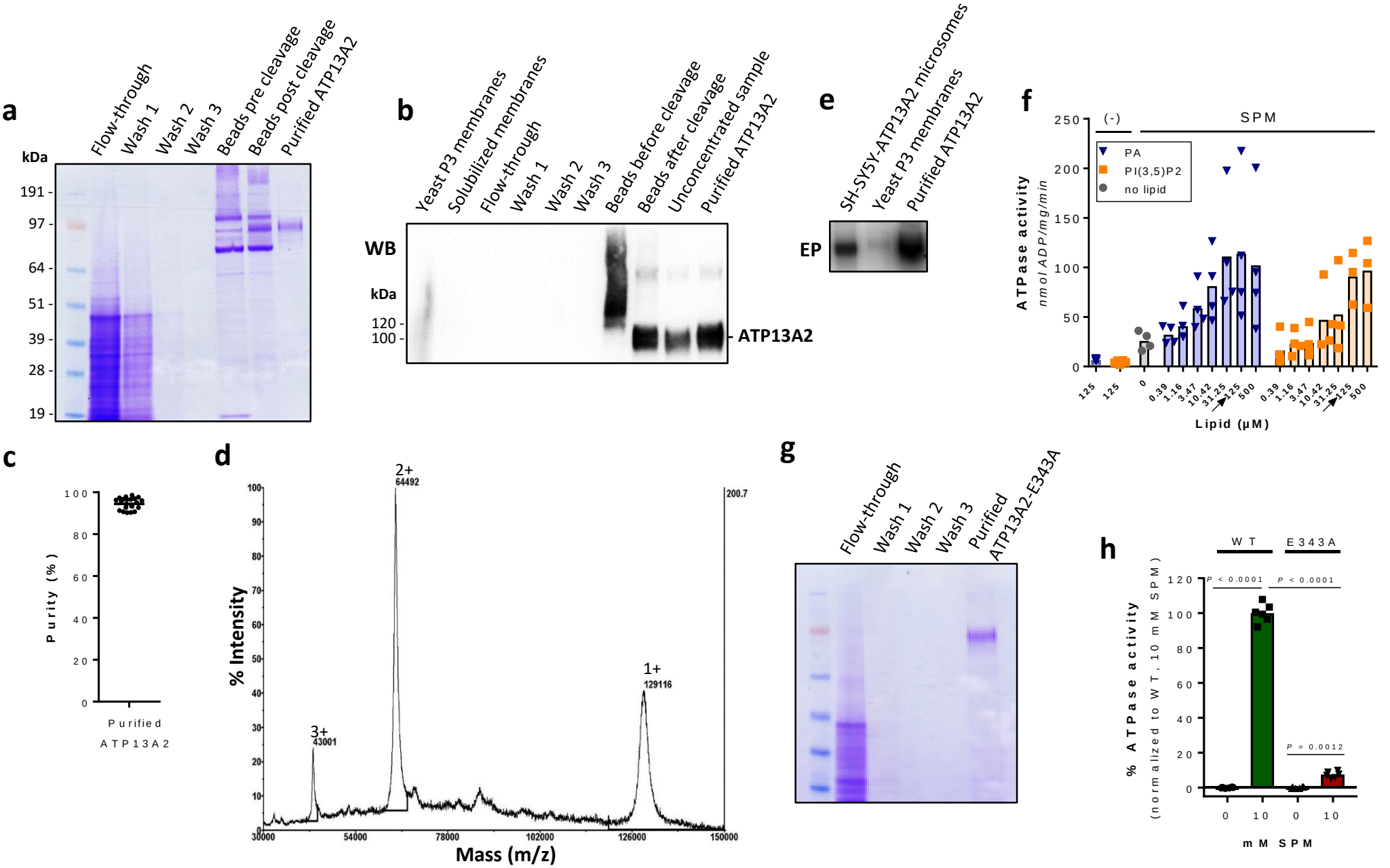

Extended Data Figure 3

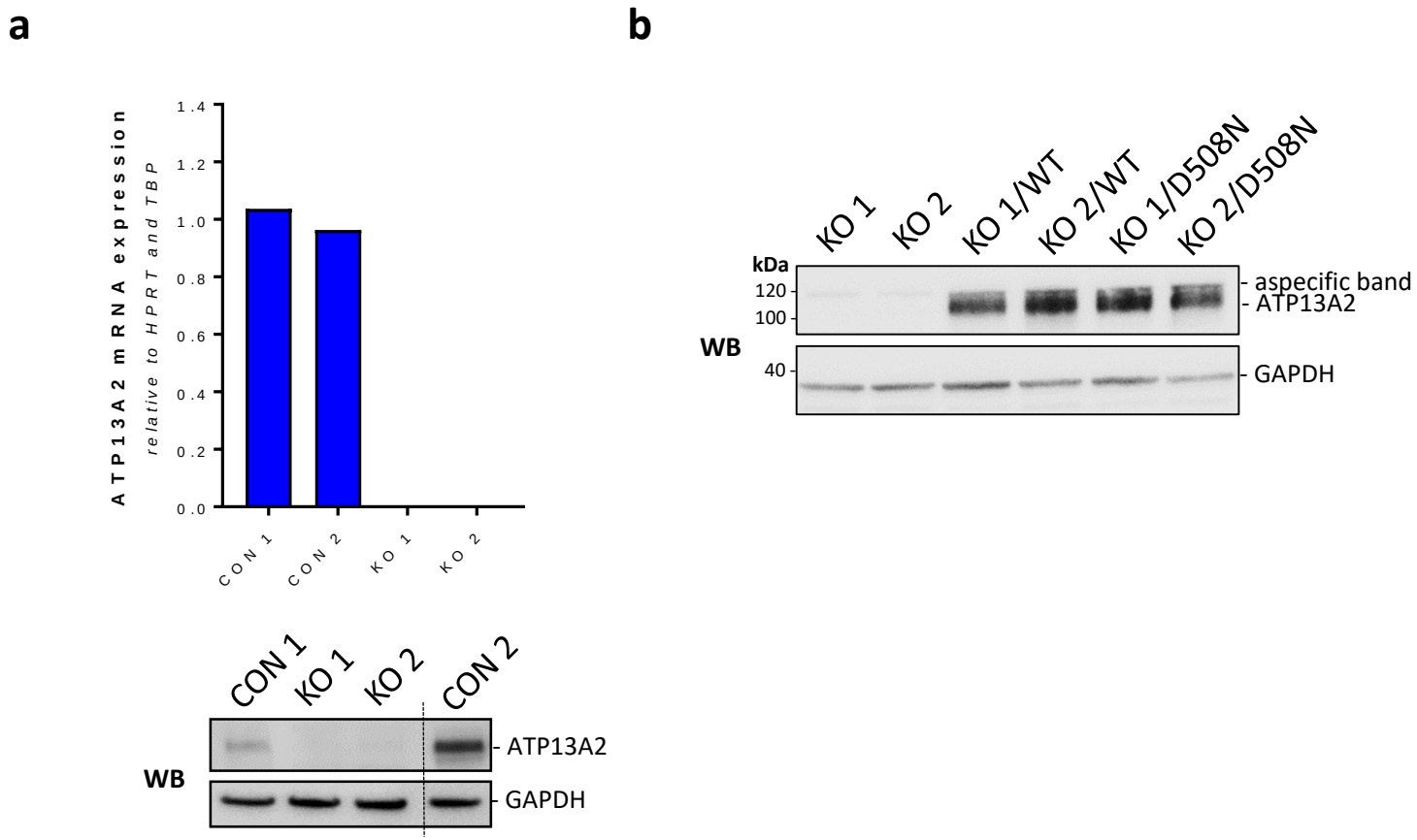

Extended Data Figure 4

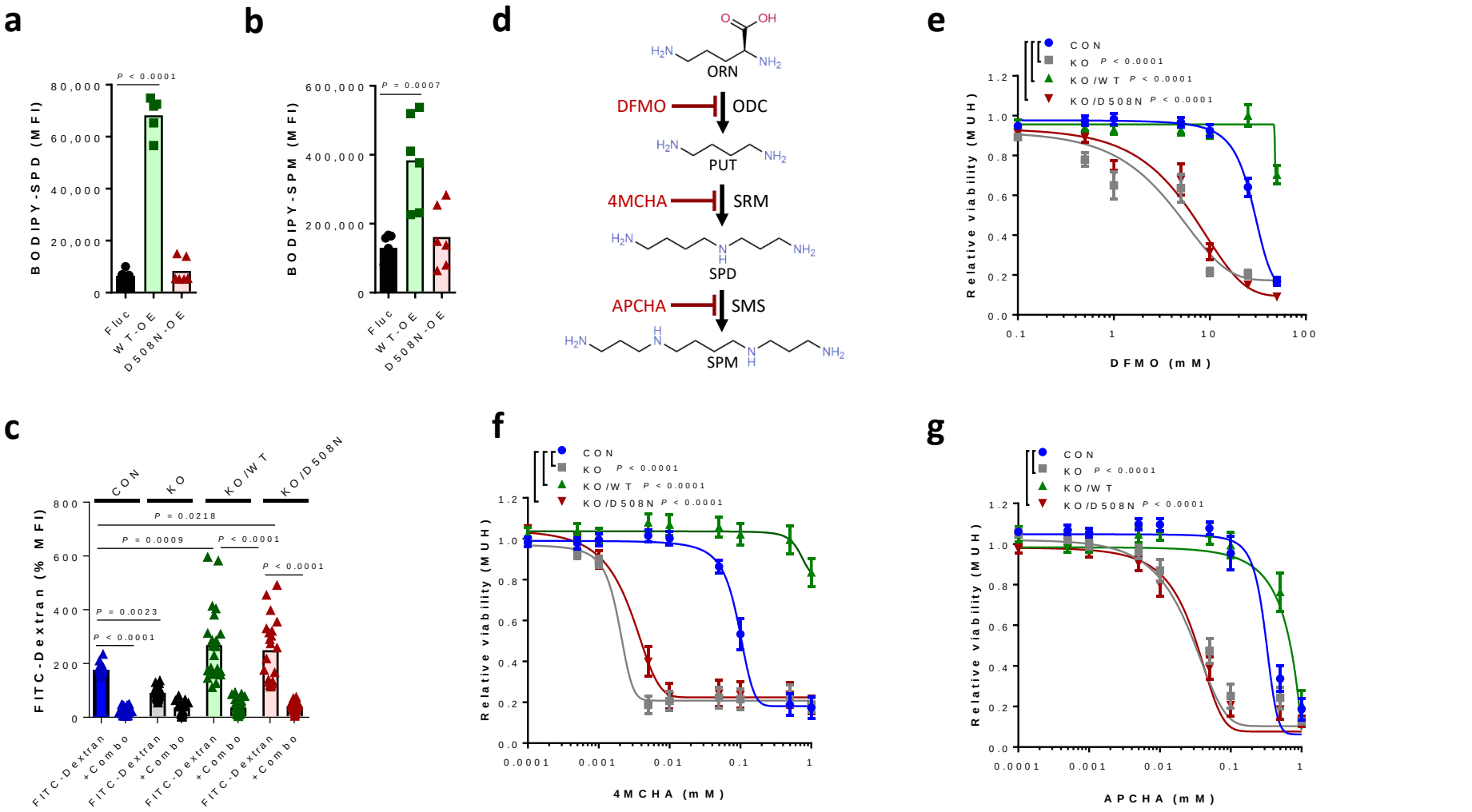

Extended Data Figure 5

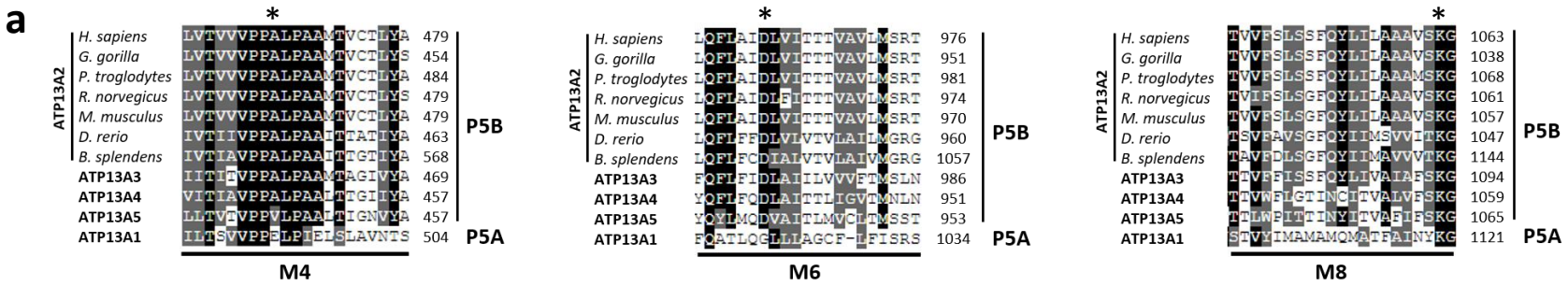

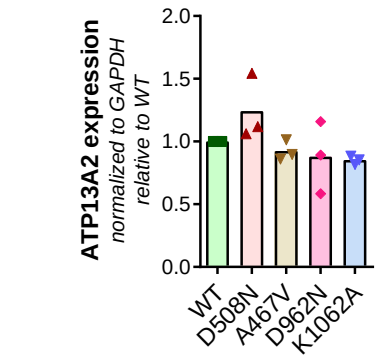

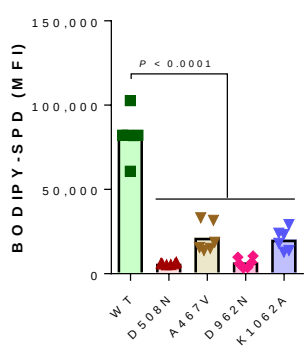

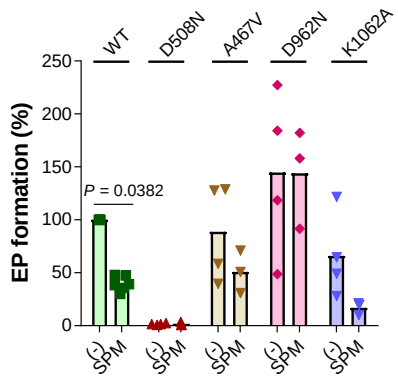

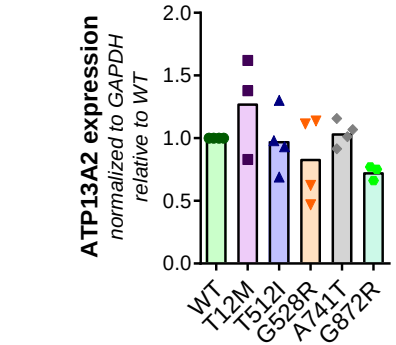

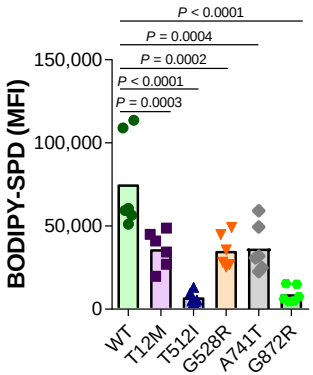

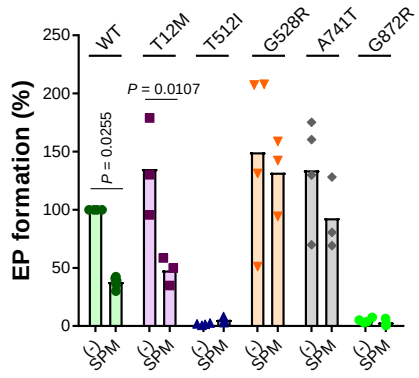

Extended Data Figure 6

a

	Source	K ± SEM (s^{-1}) ATP sensitivity	K ± SEM (s^{-1}) ATP/SPM sensitivity
ATP13A2 WT	Microsomes	0.066 ± 0.010	0.098 ± 0.008
ATP13A2 D962N	Microsomes	0.022 ± 0.019	0.020 ± 0.012
ATP13A2 WT	Purified protein	0.050 ± 0.012	0.136 ± 0.030
ATP13A2 E343A	Purified protein	0.035 ± 0.031	0.039 ± 0.015

b

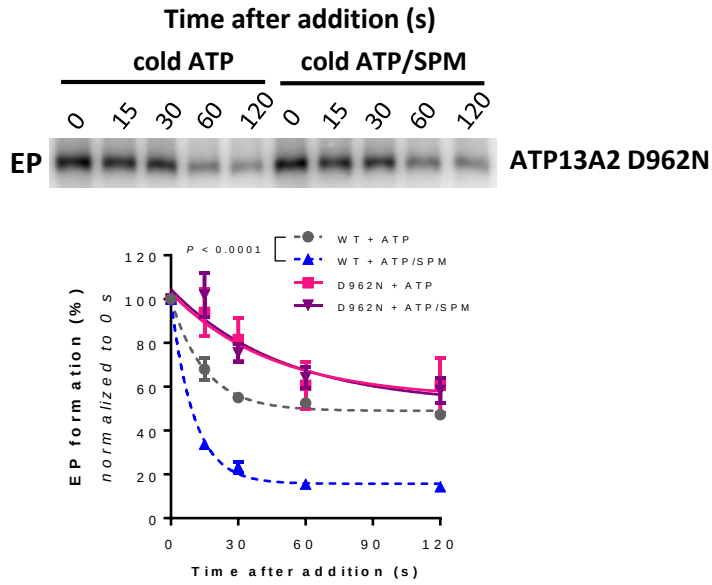

Extended Data Figure 7

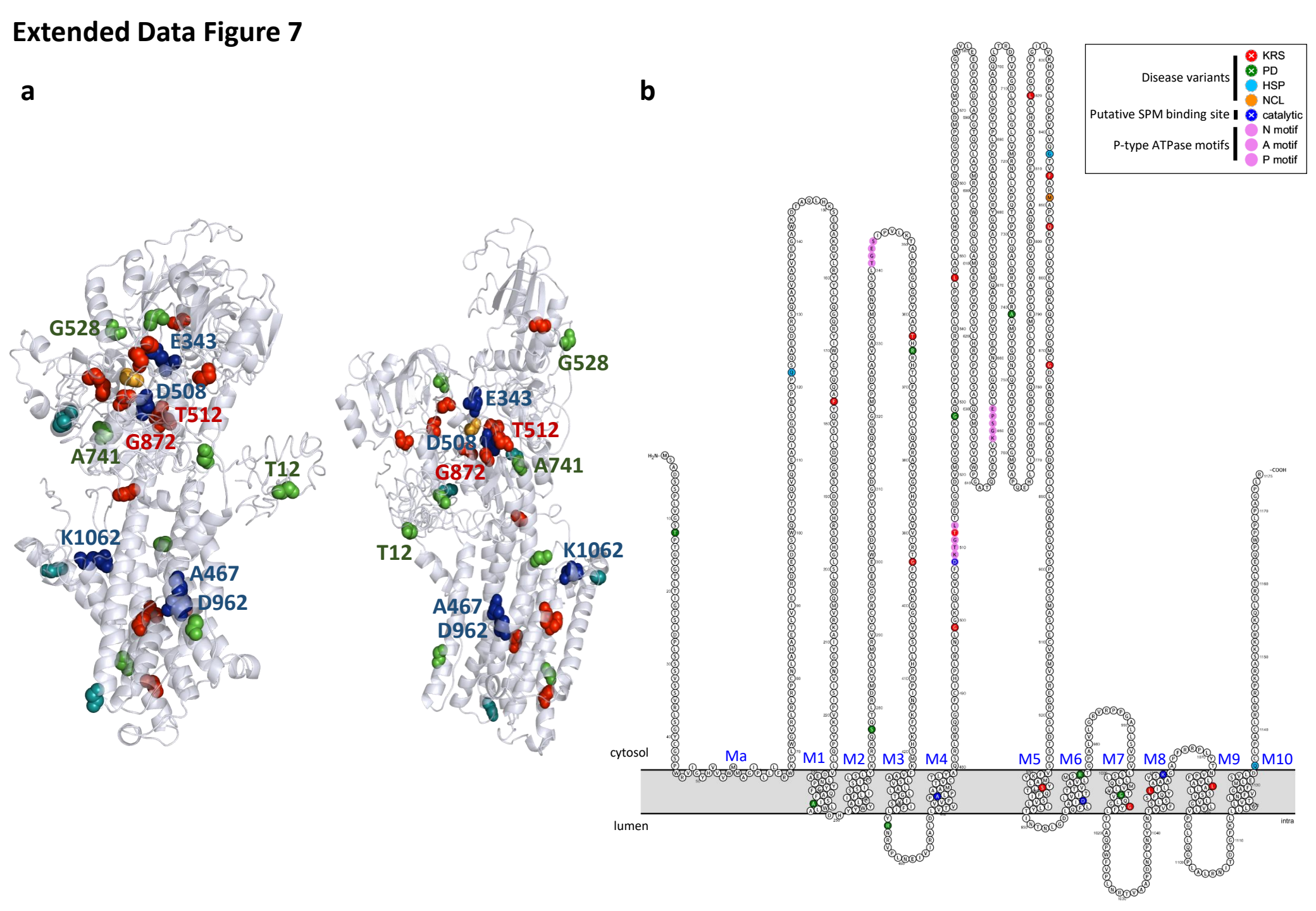

Extended Data Figure 8

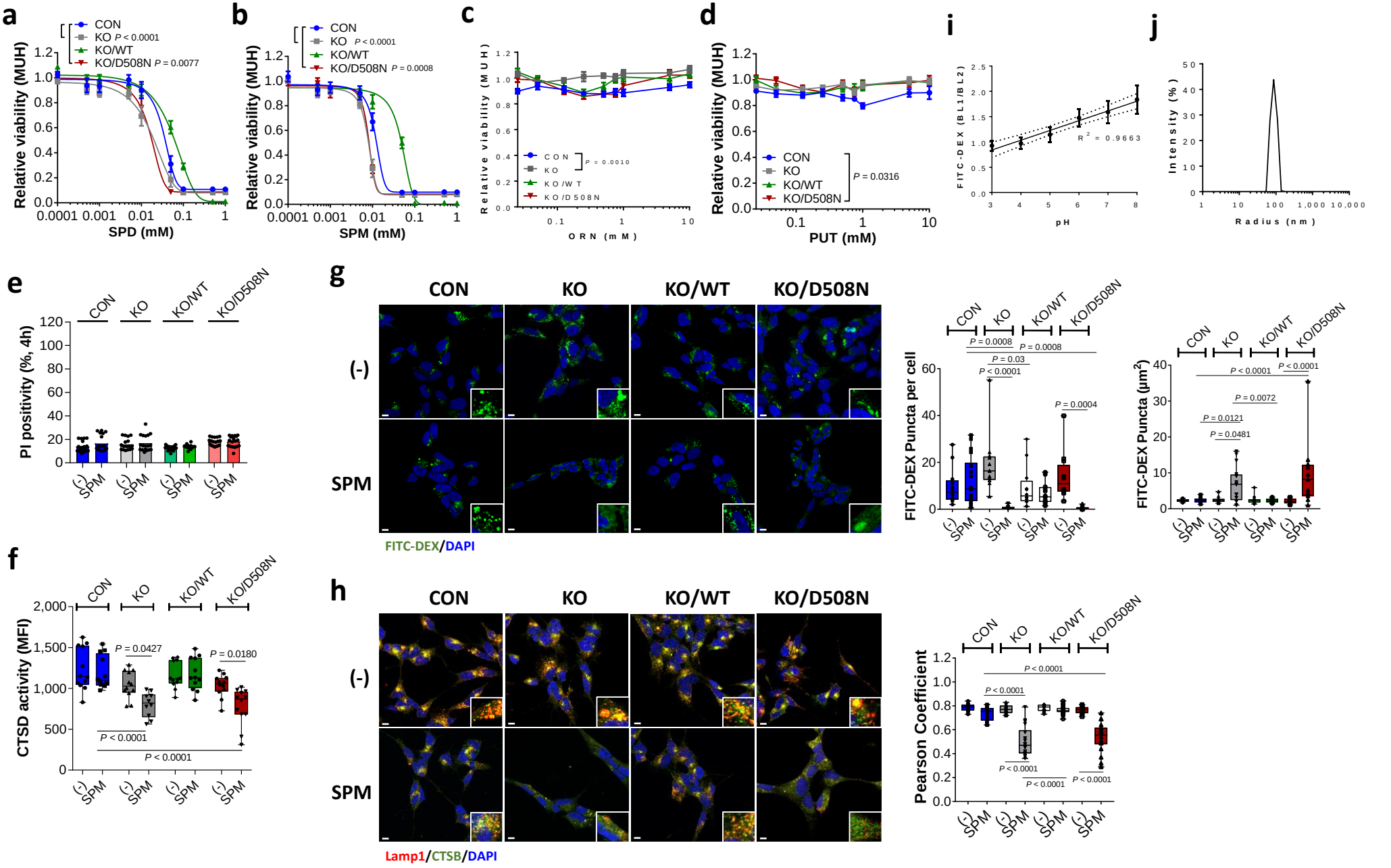

Extended Data Figure 9